

Design of J-PARC Neutrino Beamline  
and R&D of Beam Monitors

Kenji Tanabe  
Department of Physics, University of Tokyo  
January, 2004

## Abstract

The J-PARC-Kamioka long baseline neutrino oscillation experiment is a next generation long baseline neutrino oscillation experiment. A high intensity narrow band neutrino beam is produced by a high intensity proton beam.

In the J-PARC neutrino beam line, the beam power is more than 100 times higher than that in K2K. Such a high intensity proton beam induces large radiation dose. The superconducting magnets are used to bend the 50GeV proton beam by more than  $80^\circ$  toward the SK. To protect the superconducting magnets from quenching, the beam loss is strictly limited in the arc section. It is important for the designs of the beam line components to reduce the beam loss against the high intensity proton beam.

We have carried out the beam line simulation based on Geant4. We have estimated the beam loss including the secondary shower particles, and optimized the design of the beam line components.

We have also started the R&D of the Segmented Secondary Emission Monitor (SSEM) as a beam profile monitor for the J-PARC neutrino beam line. To check the basic response, we have carried out two beam tests at the K2K neutrino beam line. We test the five metal materials as the cathode electrodes, and have found that these metals have similar secondary emission efficiencies. In the second beam test, using the titanium 2mm wide strips, we demonstrate the beam profile measurement with the SSEM.

# Contents

<b>1</b>	<b>Introduction</b>	<b>9</b>
1.1	Neutrino Mass and Neutrino Oscillation . . . . .	9
1.2	Atmospheric Neutrino Experiments . . . . .	11
1.3	K2K Long Baseline Neutrino Oscillation Experiment . . . . .	12
<b>2</b>	<b>J-PARC-Kamioka Long Baseline Neutrino Oscillation Experiment</b>	<b>13</b>
2.1	Overview . . . . .	13
2.2	J-PARC Neutrino Facility . . . . .	14
2.3	Off-Axis Neutrino Beam . . . . .	14
2.4	Near/Far Neutrino Detector . . . . .	16
<b>3</b>	<b>J-PARC Neutrino Beamline</b>	<b>18</b>
3.1	Overview of Primary Proton Beamline . . . . .	18
3.1.1	Preparation Section . . . . .	19
3.1.2	Arc Section . . . . .	21
3.1.3	Focusing Section . . . . .	21
3.2	Beam Monitors . . . . .	23
<b>4</b>	<b>Simulation Study of Primary Proton Beamline</b>	<b>26</b>
4.1	Simulation Setup . . . . .	27
4.2	Beam Loss Estimation . . . . .	29
4.3	Radiation Dose of Magnets in the Preparation Section . . . . .	30
4.4	Optimization of Design Parameters for Collimators . . . . .	34
4.5	Radiation Shield at the Exit of the Preparation Section . . . . .	39
4.6	Summary . . . . .	44

<b>5</b>	<b>R&amp;D of the Segmented Secondary Emission Monitor</b>	<b>45</b>
5.1	Principle of the Secondary Emission Monitor . . . . .	46
5.2	The requirements for the design of the SSEM . . . . .	49
5.3	Beam Test at the K2K Neutrino Beamline . . . . .	58
5.3.1	The 1st beam test . . . . .	58
5.3.2	The 2nd beam test . . . . .	67
5.4	Summary and Discussion . . . . .	74
<b>6</b>	<b>Conclusion</b>	<b>76</b>

# List of Figures

1.1	The zenith angle distributions observed in Super-Kamiokande [2]. . . . .	12
2.1	Overview of J-PARC-Kamioka experiment. . . . .	14
2.2	Accelerator of J-PARC. . . . .	15
2.3	a schematic of the off-axis neutrino beam. . . . .	16
2.4	kinematics of off-axis neutrino beam. . . . .	17
3.1	Assumed beam loss in the primary proton beamline. . . . .	19
3.2	The components in the preparation section. . . . .	20
3.3	The optics parameters for the preparation section and a part of the arc section. . . . .	22
3.4	The components in the focusing section. . . . .	23
3.5	The optics parameters for the focusing section and a part of the arc section. . . . .	24
3.6	The candidates of beam monitor position. . . . .	25
4.1	Event display. . . . .	27
4.2	The phase space distribution at the extraction point. . . . .	28
4.3	The energy dropped by the incident protons and shower particles to each component of the beamline. . . . .	29
4.4	The spatial distribution of the energy deposited in the PH1. . . . .	31
4.5	The fraction of the energy deposited within 5-cm thick iron around the magnet aperture. . . . .	32
4.6	The total radiation dose a year in 5-cm thick iron. . . . .	33
4.7	The total radiation dose a year at the location where the maximum energy loss (joule/cm <sup>3</sup> ) occurs. . . . .	33
4.8	Shape of the collimators. . . . .	35

4.9	The energy deposit in the arc section with three values of the collimator thickness. . . . .	35
4.10	The energy deposit in the normal conducting magnets near the collimators for three values of the collimator thickness. . .	36
4.11	The loss of the number of beam particles (left) and the energy deposited in the arc section (right) for 4 different collimator lengths. . . . .	36
4.12	The energy deposit in the first superconducting magnet in the arc section for 4 different collimator length. . . . .	37
4.13	The energy deposit in the normal conducting magnets near the collimators (in the preparation section) for 4 different collimator length. . . . .	37
4.14	The energy deposited in the magnets and collimators (in the preparation section) for two collimator gap size. . . . .	38
4.15	The loss of the number of beam particles and the energy deposited in the arc section. . . . .	39
4.16	The phase space distributions at the collimators of the particles become lost at the arc section. . . . .	40
4.17	The phase space distributions at the PH1 and exit of the preparation section of the particles become lost at the arc section. . . . .	41
4.18	The fraction of lost particles as a function of the inner diameter of the shield. . . . .	43
4.19	The fraction of energy deposit as a function of the inner diameter of the shield. . . . .	43
5.1	a schematic view of SSEM. . . . .	46
5.2	the ratio of the number of secondary electrons and ion pairs . . . . .	49
5.3	Temperature of the electrode versus time. . . . .	53
5.4	The temperature distribution at the three seconds after a beam pulse calculated by thermal conduction only. . . . .	56
5.5	Cathode electrodes for the 1st beam test. . . . .	60
5.6	Cathode and anode electrodes for the 1st beam test. . . . .	61
5.7	The setup of the beam test. . . . .	62
5.8	Vacuum dependence of ion pump voltage. . . . .	62
5.9	Anode voltage dependence of signal height. . . . .	64
5.10	Waveform from aluminum three channels. . . . .	64
5.11	The measured beam profiles with three strips for each metal. . . . .	65

5.12	The measured secondary emission efficiencies for five cathode metals. . . . .	66
5.13	Cathode and anode electrodes for the second beam test. . . .	68
5.14	Signal wave form from titanium strips after the pulse transformer and 14dB attenuator. . . . .	69
5.15	ADC count from 19 titanium strips. . . . .	71
5.16	The measured beam profiles for three beam positions. . . . .	71
5.17	The anode voltage dependence of the measured profile. . . . .	73

# List of Tables

2.1	Comparison of accelerators used for the neutrino beam generation. . . . .	15
3.1	Collimator size. . . . .	21
4.1	The fraction of the lost beam particles in the preparation and arc section, and the total energy deposit in the arc section and that in the first superconducting magnet with the baseline collimators (Table 3.1) and without the collimators, respectively.	34
4.2	The fraction of the lost beam particles in the preparation and arc sections, and the energy deposited in the arc total and first superconducting magnet, without the tunnel filler shield. . . .	42
5.1	Thickness of materials equivalent to $10^{-5}\lambda_{\text{int}}$ . . . . .	50
5.2	The amount of expected signal charge . . . . .	53
5.3	Estimated temperature rise due to one beam pulse, as well as the used parameters for the calculation. . . . .	55
5.4	The estimated temperature in the stationary state from thermal radiation. . . . .	57
5.5	Cathode materials for the 1st beam test. . . . .	59
5.6	Cathode materials for the 2nd beam test. . . . .	67
5.7	Change in the center position of measured beam profiles for three beam positions. . . . .	70
5.8	The value of one sigma of each beam profile shown in Fig.5.16.	72

# Chapter 1

## Introduction

### 1.1 Neutrino Mass and Neutrino Oscillation

The standard model defines the neutrino mass to be zero. However, recent atmospheric and solar neutrino experiments show that neutrinos have masses and have large mixings. Neutrino mass and mixing can be one of a few possible windows of the physics beyond the standard model.

Three different neutrinos are expressed as flavor eigenstates,  $\nu_e$ ,  $\nu_\mu$ , and  $\nu_\tau$ . At present, the upper limit of the masses of the three neutrino species is as follows [1].

$$\begin{aligned} m_{\nu_e} &< 3 \text{ eV} \\ m_{\nu_\mu} &< 190 \text{ keV} \\ m_{\nu_\tau} &< 18.2 \text{ MeV} \end{aligned}$$

If the neutrino has a non-degenerate mass, the neutrino oscillation is caused by the mixing of the flavor eigenstate and the mass eigenstate. The mixing of neutrinos is described by a unitary 3x3 matrix ( $U_{\alpha i}$ ) in the 3 generation case,

$$\begin{pmatrix} \nu_e \\ \nu_\mu \\ \nu_\tau \end{pmatrix} = U_{\alpha i} \begin{pmatrix} \nu_1 \\ \nu_2 \\ \nu_3 \end{pmatrix},$$

where  $\nu_e, \nu_\mu, \nu_\tau$  are the flavor eigenstates,  $\nu_1, \nu_2, \nu_3$  are the mass eigenstates.  $U_{\alpha i}$  includes the four independent parameters, 3 mixing angles,  $\theta_{12}, \theta_{23}$  and  $\theta_{31}$ , and a phase  $\delta$  as an analogy of CKM matrix in the quark sector.

For the simplicity, the oscillation probability in two generations is calculated. The mixing in two generations is described as,

$$\begin{pmatrix} \nu_\mu \\ \nu_\tau \end{pmatrix} = \begin{pmatrix} \cos \theta & \sin \theta \\ -\sin \theta & \cos \theta \end{pmatrix} \begin{pmatrix} \nu_2 \\ \nu_3 \end{pmatrix}, \quad (1.1)$$

where  $\theta$  is the mixing angle. Since neutrinos are generated via weak interactions in the flavor eigenstates, their time evolution of the state is described as mass eigenstates in following Schrödinger equation:

$$\begin{aligned} i \frac{d}{dt} \begin{pmatrix} \nu_2 \\ \nu_3 \end{pmatrix} &= H \begin{pmatrix} \nu_2 \\ \nu_3 \end{pmatrix} \\ &= \begin{pmatrix} E_2 & 0 \\ 0 & E_3 \end{pmatrix} \begin{pmatrix} \nu_2 \\ \nu_3 \end{pmatrix}. \end{aligned}$$

This equation can be solved as following:

$$\nu_i(t) = \nu_i(0) e^{-iE_i t},$$

where  $i = 2, 3$  are the indices of the mass eigenstates,  $E_i$  are energy eigenvalues. We assume the states  $\nu_i$  have common momentum  $p$  and mass  $m_i$  ( $\ll p$ ). The energy eigenvalues are approximated as:

$$E_i = \sqrt{p^2 + m_i^2} \sim p + \frac{m_i^2}{2p}. \quad (1.2)$$

If we assume a neutrino is generated as  $\nu_\mu$  at the time  $t=0$ ,  $\nu_2(0)$  and  $\nu_3(0)$  become  $\cos \theta$  and  $\sin \theta$  from Eq.1.1, respectively.

The  $\nu_\mu \rightarrow \nu_\tau$  oscillation probability at time  $t$ , or at distance  $L$ , is described as:

$$\begin{aligned} P(\nu_\mu \rightarrow \nu_\tau) &= |\nu_\mu(0)\nu_\tau(t)|^2 \\ &= |(\cos \theta \nu_2(0) + \sin \theta \nu_3(0))(-\sin \theta \nu_2(t) + \cos \theta \nu_3(t))|^2 \\ &= \sin^2 2\theta \sin^2 \left( \frac{1}{2}(E_2 - E_3)t \right). \end{aligned}$$

If we use the Eq.1.2, we can get,

$$P(\nu_\mu \rightarrow \nu_\tau) = \sin^2 2\theta \sin^2 \left( 1.27 \frac{\Delta m^2 [\text{eV}^2] L [\text{m}]}{E [\text{MeV}]} \right),$$

where we use  $\Delta m^2 = m_3^2 - m_2^2$ ,  $E \sim p$ , and  $L \sim t$ , respectively. The oscillation probability depends on  $\Delta m^2$  and mixing angle  $\theta$ . The observation of neutrino oscillation proves the existence of different mass eigenstates of neutrinos and the existence of mixing between the mass eigenstate and flavor eigenstate.

## 1.2 Atmospheric Neutrino Experiments

Atmospheric neutrinos are produced as decay products in hadronic showers generated by the interaction between primary cosmic rays and the upper atmosphere. The interaction of primary cosmic rays with the nuclei in upper atmosphere creates secondary pions and kaons. Atmospheric neutrinos are produced from decay of these pions and kaons as following:

$$\begin{aligned} \pi^\pm / K^\pm &\rightarrow \mu^\pm \nu_\mu (\bar{\nu}_\mu) \\ \mu^\pm &\rightarrow e^\pm \bar{\nu}_\mu \nu_e (\nu_\mu \bar{\nu}_e). \end{aligned}$$

The expected flux ratio  $(\nu_\mu + \bar{\nu}_\mu)/(\nu_e + \bar{\nu}_e)$  is 2. It is predicted with an uncertainty of less than 5%.

This ratio has been measured by several underground experiments. These measurements are compared to expectations based on Monte Carlo simulations as following:

$$R \equiv \left( \frac{\nu_\mu + \bar{\nu}_\mu}{\nu_e + \bar{\nu}_e} \right)_{obs} / \left( \frac{\nu_\mu + \bar{\nu}_\mu}{\nu_e + \bar{\nu}_e} \right)_{MC}.$$

Kamiokande, IMB, Super-Kamiokande and Soudan-2 reported that  $R$  was significantly smaller than unity. Neutrino oscillations have been suggested to explain this small values of  $R$ .

Furthermore, the zenith angle distribution of the atmospheric neutrinos was measured, and the Super-Kamiokande experiment reported evidence for oscillations of the atmospheric neutrinos. Figure 1.1 shows the recent result of Super-Kamiokande experiment in 1,489 live-day [2]. From this result, the allowed region of parameters is  $\sin^2 2\theta > 0.92$ ,  $1.6 \times 10^{-3} < \Delta m^2 < 3.9 \times 10^{-3} \text{ eV}^2$  at 90% confidence level.

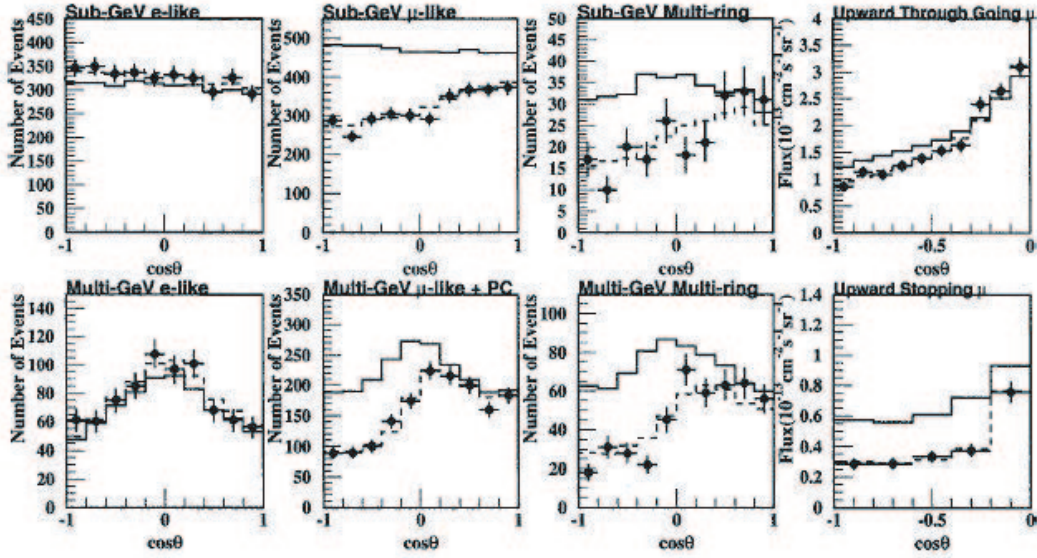


Figure 1.1: The zenith angle distributions observed in Super-Kamiokande [2].

### 1.3 K2K Long Baseline Neutrino Oscillation Experiment

The KEK to Kamioka long-baseline neutrino experiment (K2K) is the first accelerator-based experiment with hundreds of km neutrino path length. In the accelerator experiments, the neutrino flux and their flavor is well known (almost pure  $\nu_\mu$ ). The existence of neutrino oscillations can be confirmed very clearly.

In the K2K experiment, the neutrino beam is produced by a 12 GeV proton beam from the KEK proton synchrotron. The mean neutrino energy is 1.3 GeV and the baseline is about 250 km. This is suitable to confirm the parameter region suggested by atmospheric neutrino experiments. Its first result already show the indication of the neutrino oscillation [3].

# Chapter 2

## J-PARC-Kamioka Long Baseline Neutrino Oscillation Experiment

### 2.1 Overview

The J-PARC-Kamioka Long Baseline Neutrino Oscillation Experiment is a next generation long baseline neutrino oscillation experiment. The baseline length is about 295km from J-PARC (in Tokai village) to the far neutrino detector, Super-Kamiokande (SK) in Kamioka mine (Fig.2.1). The neutrino energy is tuned to the oscillation maximum at  $\sim 0.7$  GeV for the distance of 295km and  $\Delta m^2 \sim 3 \times 10^{-3}$  eV<sup>2</sup>.

In the J-PARC neutrino beamline, the proton beam power is more than 100 times higher than that in K2K. A high intensity neutrino beam produced by a high intensity proton beam allows us to measure the neutrino oscillation parameters precisely. In the phase 1 experiment, the physics goals are [4],[5]:

- A factor of 20 more sensitive search in the  $\nu_e$  appearance (at  $\Delta m^2 \sim 3 \times 10^{-3}$  eV<sup>2</sup> down to  $\sin^2 2\theta_{13} \sim 0.006$ ).
- Precise determination of neutrino oscillation parameters by the  $\nu_\mu$  disappearance (down to  $\delta(\Delta m_{23}^2) = 10^{-4}$  eV<sup>2</sup> and  $\delta(\sin^2 2\theta_{23}) = 0.01$ ).
- Search for a sterile component in  $\nu_\mu$  disappearance by detecting the neutral current events.



Figure 2.1: Overview of J-PARC-Kamioka experiment.

## 2.2 J-PARC Neutrino Facility

The layout of J-PARC Facility is shown in Fig.2.2. The proton beam is fast extracted from the 50GeV-PS. The extracted proton beam is bent more than  $80^\circ$ , and transported to the neutrino production target. The neutrino beam in J-PARC is almost  $\nu_\mu$  from the  $\pi$  meson decay. The generated  $\pi$ s at the target are focused to forward direction by three electromagnetic horns. In the decay volume, most of  $\pi$ s decay into  $\nu_\mu$ s and  $\mu$ s in flight. We describe the neutrino beam in J-PARC in the following section.

In Table 2.1, accelerator parameters for the neutrino beam generation at K2K and J-PARC neutrino experiments are summarized. The beam power of J-PARC is more than 100 times higher than that in K2K. The intensity of the low energy neutrino is almost proportional to the proton beam power.

## 2.3 Off-Axis Neutrino Beam

The neutrino beam in J-PARC adopts the off-axis scheme. In the off-axis beam, the detector is placed at a few degree (Off-Axis angle) off from the beam axis as shown in Fig.2.3.

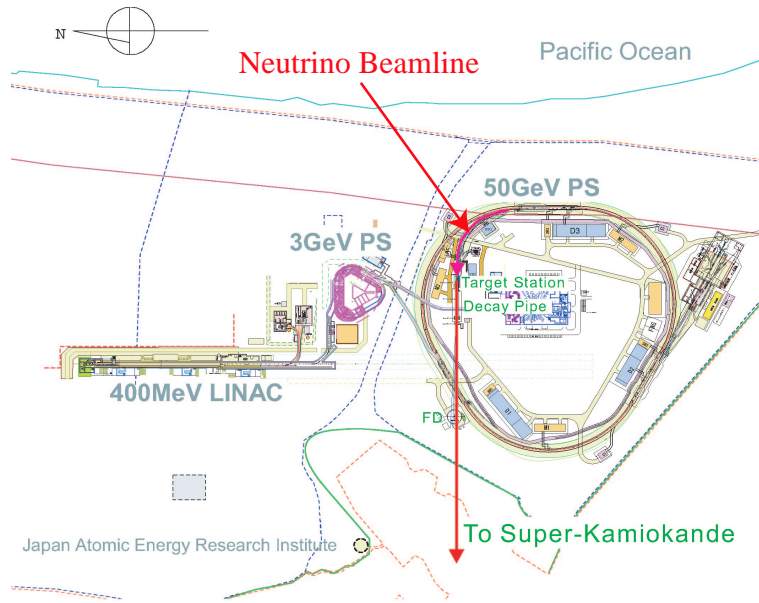


Figure 2.2: Accelerator of J-PARC.

	K2K	J-PARC
Kinetic Energy	12 GeV	50 GeV
Beam Intensity	$6.0 \times 10^{12}$ ppp.	$3.3 \times 10^{14}$ ppp.
Repetition Rate	1pulse/2.2sec	1pulse/3.5sec
Beam Power	0.0052MW	0.75MW
Spill Width	1.1 $\mu$ sec. (9 bunches/pulse)	$\sim 5\mu$ sec. (8bunches/pulse)

Table 2.1: Comparison of accelerators used for the neutrino beam generation. ppp stand for the number of protons per pulse.

Considering the kinematics of the  $\pi$  decay, with a finite decay angle, the neutrino energy becomes almost independent of parent  $\pi$  energy (Eq.2.1, Fig.2.4). The off-axis beam can produce the high intensity neutrino beam with a narrow energy spread. The high energy neutrinos are background sources via the inelastic reaction. In addition, inelastic reaction produce the  $\pi_0$ s that are the main background for the electron appearance search. These physics conditions prefers the high intensity narrow band low energy neutrino beam.

$$E_\nu = \frac{m_\pi^2 - m_\mu^2}{2(E_\pi - p_\pi \cos \theta)} \quad (2.1)$$

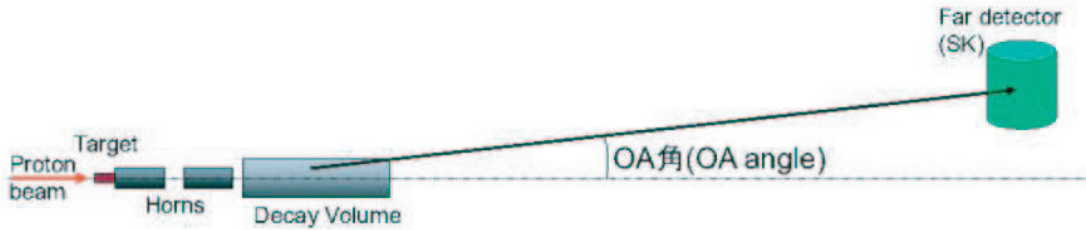


Figure 2.3: a schematic of the off-axis neutrino beam.

## 2.4 Near/Far Neutrino Detector

The two different neutrino detector systems are planned to install at the 280m from the target. One is placed at the on-axis line. The main purpose of this detector is to measure the neutrino beam direction, intensity and energy spectrum. The other is placed at the off-axis line to measure the energy spectrum and the  $\nu_e$  contamination for the neutrino beam toward SK.

In addition, the intermediate detector is planned to place at the 2km from

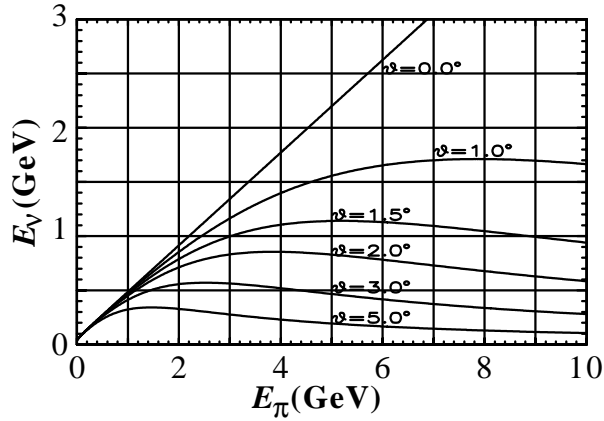


Figure 2.4: kinematics of off-axis neutrino beam. horizontal axis is the energy of  $\pi$ s and vertical is  $\nu_\mu$ s.

the neutrino target. At that distance, the neutrino energy spectrum becomes almost the same as those at SK without neutrino oscillation. This 2km detector improves the precision of the neutrino energy spectrum projection at SK.

The design of these detectors are underway by the experimental group.

This experiment uses the world largest water Cerenkov detector, Super-Kamiokande (SK), as the far detector. SK is already operating. SK has excellent performance in detecting low energy neutrinos, and the  $e/\mu$  identification capability.

# Chapter 3

## J-PARC Neutrino Beamline

### 3.1 Overview of Primary Proton Beamline

We describe the overview of the primary proton beamline in J-PARC. The details can be found elsewhere [6].

The primary proton beamline transfers the extracted proton beam from 50GeV-PS to the neutrino production target. It consists of three sections, the preparation section, the arc section, and the final focusing section. The arc section aims to bend the 50GeV proton beam about  $80^\circ$ . Since the curvature of the arc section is as small as 100m due to the geometrical limitation of the site, superconducting magnets are adopted for the arc section. The arc section is the world first beamline made of combined function superconducting magnets as described in the following section.

It is extremely important to control the beam loss for the high intensity proton beam to achieve stable operation and safe maintenance. However, it is hardly possible to estimate absolute beam loss by calculation. Then in the primary proton beamline, the upper limit of the beam loss is set by hand for the each section as shown in Fig.3.1. In particular, the beam loss in the arc section is limited to 1W/m to protect the superconducting magnets from quenching and to keep the activation of equipments below hands-on maintenance level. To achieve this requirement, it is important to scrape beam halo off with collimators in the preparation section. In the following, we describe outlines of each part of the beamline.

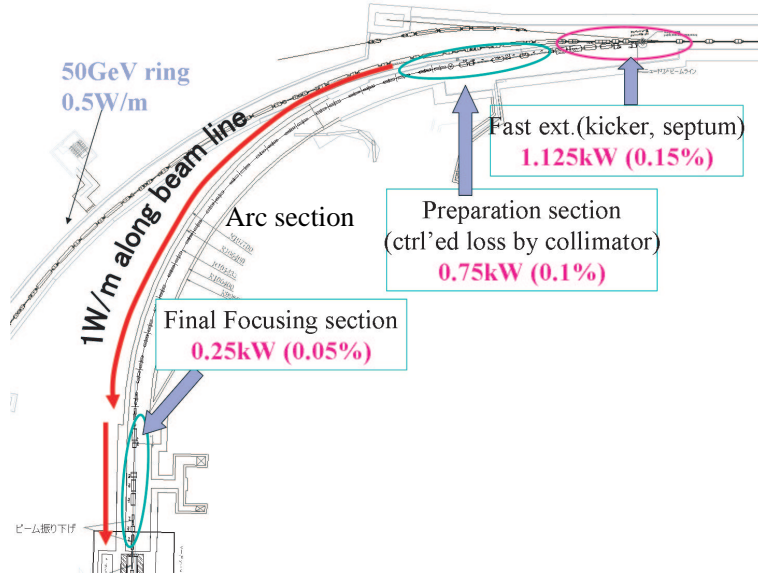


Figure 3.1: Assumed beam loss in the primary proton beamline.

### 3.1.1 Preparation Section

The preparation section consists of normal conducting magnets and collimators. This section matches the beam with the suitable condition to pass through the arc section. In this section, beam halo is scraped off to protect the superconducting magnets in the arc section. The beam loss in this section is assumed to be relatively high (750W in total). The aperture of magnets and collimators in the preparation section is determined to accept the  $60\pi$  mm · mrad beam, while the designed value of the extracted beam emittance is  $6\pi$  mm · mrad at 50GeV. The beam halo whose emittance is larger than this is scraped off by both the magnets and collimators.

Figure 3.2 shows the components in the preparation section. To scrape the beam halo off in the limited space of the preparation section, four collimators are placed to fill up as much drift space as possible. The baseline design of collimators is listed in Table 3.1. We describe in Chapter 4 about optimization of these design parameters and estimation of beam loss using the beamline simulation.

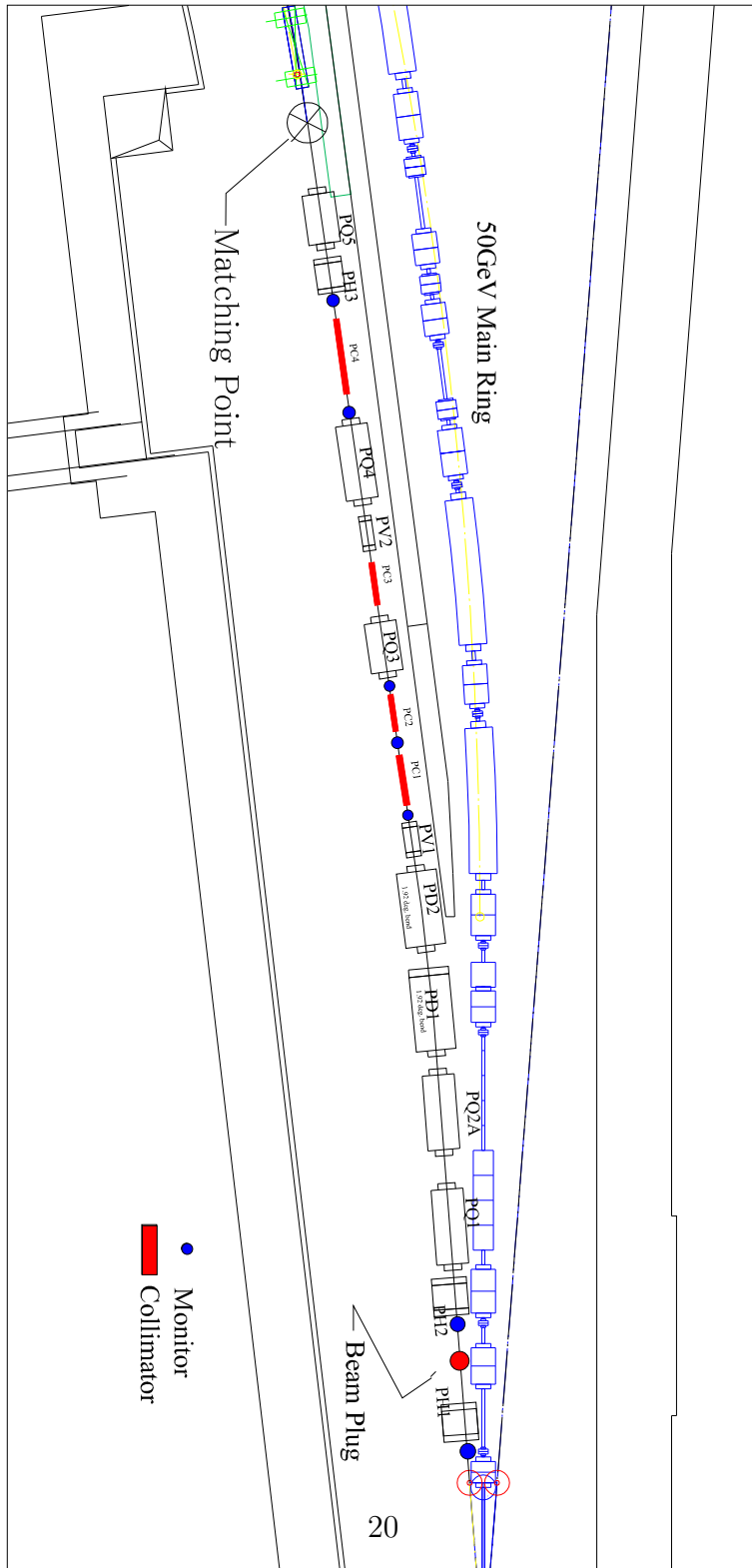


Figure 3.2: The components in the preparation section.

Name	Length [m]	Gap Height [mm]	Gap Width [mm]
PC1	2.	39	115
PC2	1.45	31	121
PC3	1.7	78	109
PC4	3.	95	64

Table 3.1: Collimator size. The gap size is determined to accept  $60\pi$  mm · mrad beam.

### 3.1.2 Arc Section

The arc section consists of superconducting combined function (CF) magnets. The CF magnet has overlapped dipole and quadrupole magnetic fields, like

$$\begin{aligned} B_x &= Q * y \\ B_y &= D + Q * x, \end{aligned}$$

where  $D$  is the dipole component and  $Q$  is the quadrupole field gradient. One CF magnet works as both bending and focusing magnet. By using CF magnets instead of separated dipole and quadrupole superconducting magnets, the arc section is able to have larger number of FODO cells with smaller number of magnets. As a result, the beam size in the arc section becomes smaller. The admittance of the arc section is increased with the same aperture. As described before, it is important to reduce the beam loss in the arc section. This increase of admittance is one of the main advantage of CF magnets. The calculated admittance is as large as  $204 \pi$  mm · mrad for horizontal, and  $294 \pi$  mm · mrad for vertical [6].

Figure 3.3 shows the designed optics for the preparation and a part of the arc section. In the arc section, the optics are designed to be periodic and to have the  $90^\circ$  phase advance for every cell. This means that, for every four cells, the optics parameters are same. In the time of beam tuning, by checking this condition, we can check whether the beam is matched with designed optics.

### 3.1.3 Focusing Section

The focusing section consists of normal conducting magnets. In this section, the beam is focused to fit the neutrino target radius, i.e. 15mm. Before

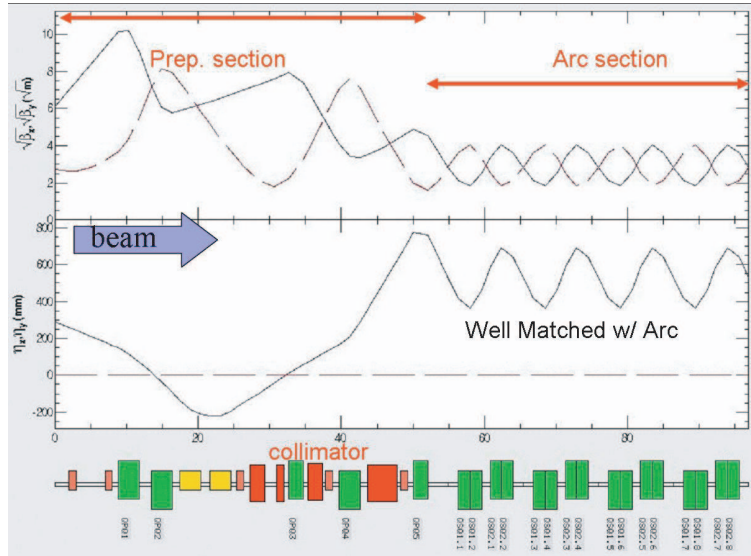


Figure 3.3: The optics parameters for the preparation section and a part of the arc section. The horizontal axis is length along the orbit in meter. Upper graph shows the squared  $\beta$  functions and lower is  $\eta$  function. Solid blue lines correspond to the horizontal parameter and dashed red lines vertical.

the focusing, the beam must be defocused once. The assumed beam loss is relatively large, 250W. The acceptance of this section is the same as the preparation section,  $60\pi$  mm · mrad. Figure 3.4 is the schematic side view of the focusing section. The two vertical bending magnets, named FV1 and FV2, bend the beam downward to cover the off-axis angle from 2 degree to 3 degree.

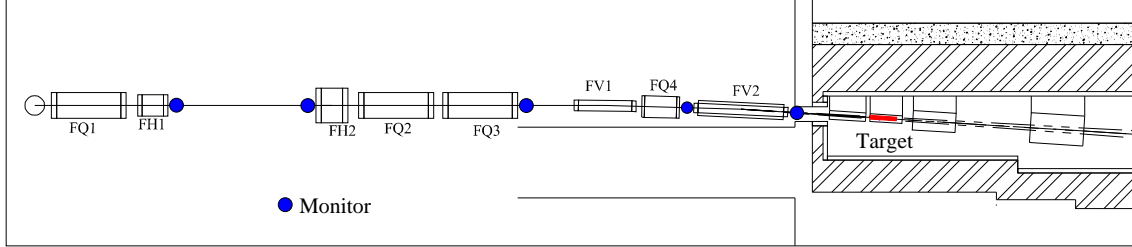


Figure 3.4: The components in the focusing section.

Figure 3.5 shows the designed optics for the focusing section. In the end of the focusing section, to fit the beam size to the neutrino target, the horizontal and vertical beta functions become same. With the fixed size of the target, the beam optics in the focusing section depends on the absolute value of the beam emittance. Figure 3.5 shows the optics for  $6\pi$  mm · mrad beam.

## 3.2 Beam Monitors

Beam monitors will be installed along the primary beam line to monitor and to control the beam conditions during the experiment. At present, four kinds of beam monitors listed below are considered to be installed:

- Intensity Monitor,
- Position Monitor,
- Profile Monitor, and
- Loss Monitor.

About the profile monitor, we describe the status of R&D in Chapter 5

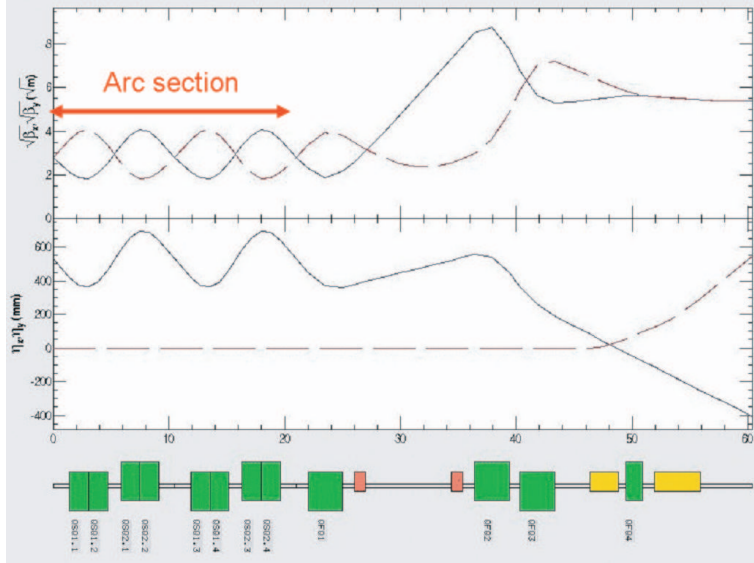


Figure 3.5: The optics parameters for the focusing section and a part of the arc section. This shows the parameters for  $6\pi$  mm · mrad beam.

In Fig.3.2, Fig.3.4, and Fig.3.6, we show the places to install the monitors. Here we will install the set of monitors, profile and position monitors, in each place.

As described before, in the arc section, the optics for every four cells become same. If the matching between the preparation section and arc section is perfect, the optics becomes same for every cell. By putting profile monitors at the positions in Fig.3.6, we can check these conditions.

Due to the space limitation and radiation environment, we may not be able to place beam monitors near the neutrino target. With the monitors in the focusing section, we need to estimate the beam size at the target. This is very important for the experiment, since the beam profile on the target can affect neutrino beam characteristics. For example, if the beam size is larger than the target diameter, the neutrino yield is decreased. If the beam profile is asymmetric, it may cause systematic error on the neutrino beam spectrum. In addition, beam profile measurement is crucial for the neutrino facility because the target would be destroyed by the heat concentration with too focused beam.

With beamline simulations, these candidates of positions and types of monitors will be checked.

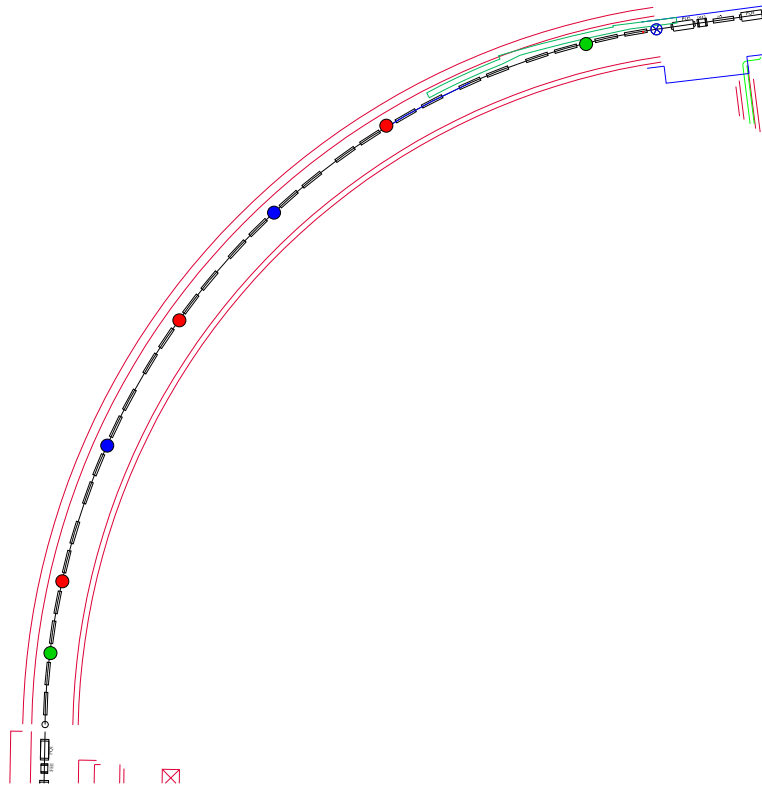


Figure 3.6: The candidates of beam monitor position. The positions of same colors has a same optics parameters.

## Chapter 4

# Simulation Study of Primary Proton Beamline

In the J-PARC neutrino beamline, the high intensity proton beam causes large radiation dose. As described in the previous chapter, to protect the superconducting magnets in the arc section, beam loss in the arc section is restricted tightly. To estimate the beam loss generated from the beam halo, we have carried out the beamline simulations based on Geant4[7].

In the optics design, the emittance of beam core from 50-GeV main ring is  $6 \pi \text{mm} \cdot \text{mrad}$  and momentum dispersion is about 0.3%. The designed acceptance of preparation section is  $60 \pi \text{mm} \cdot \text{mrad}$  [6]. This value is much larger than the beam core. The admittance of arc section is still larger than preparation section. To control the energy deposit at the arc section, the beam halo is scraped off in the preparation section. In the preparation section, therefore, relatively large beam loss is assumed. We have checked not only the beam loss at the superconducting magnets, but also the radiation dose for the normal conducting magnets. In the following, we have varied the design parameters for some components, and estimated the effect on the beam loss to optimize the design of components.

## 4.1 Simulation Setup

We describe the setup of the Geant4 simulation. Figure 4.1 shows the event display of the simulation. In the simulation, we put magnets according to the beamline design. We assume the magnets consist of iron and they are 30cm and 20cm thick around the aperture in the normal and superconducting magnets, respectively. The length of the magnet and the strength of the magnetic field are the designed value with SAD calculation.[6] Here these magnets have the uniform magnetic fields. We do not take into account the distortion of the edge field.

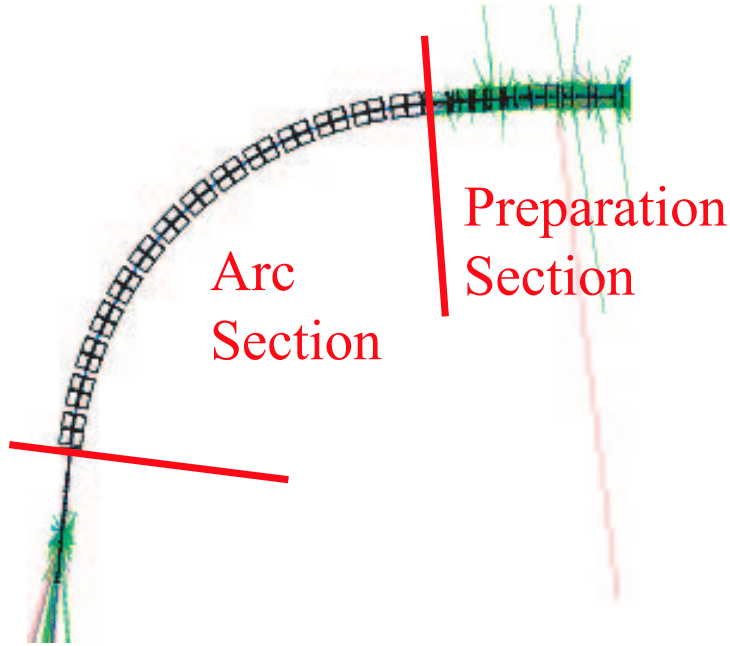


Figure 4.1: Event display.

We generate a proton beam at the extraction point. In this study, to estimate the effect of the beam halo, the generated beam emulates the beam halo by setting the beam size much larger than that of the designed beam core. The generated beam halo parameters are assumed that the kinetic energy of the incident protons is 50 GeV, the momentum dispersion is  $dp/p = 0.02$ , and the beam emittance is  $\epsilon = 200\pi \text{ mm} \cdot \text{mrad}$ , while the designed beam core parameters are  $dp/p = 0.003$ ,  $\epsilon = 6\pi \text{ mm} \cdot \text{mrad}$ . The shape of

the generated beam halo is the ellipse in the phase space. We calculate this beam shape using the designed optics parameters of the extracted beam from 50GeV MR. The incident protons are generated uniformly over this phase space ellipse.

Figure 4.2 shows the phase space distribution at the extraction point. The shape of the assumed beam halo is shown with the green line ( $\epsilon = 200\pi$  mm·mrad). To check whether the particles outside the  $\epsilon = 200\pi$  mm·mrad cause the beam loss in the arc section, we generate the beam halo with the parameters of  $\epsilon = 500\pi$  mm·mrad,  $dp/p = 0.02$  (blue line), and we plot the particles passing through the preparation section with black dots in this figure. The most of the black dots are inside the green ellipse. This result indicates that the beam halo with the size of  $\epsilon = 200\pi$  mm·mrad contains the most of the particles which can be lost in the arc section.

In the following study, these beam halo parameters are fixed, and the relative variation of the beam loss is estimated when we change the design parameters of the beamline components.

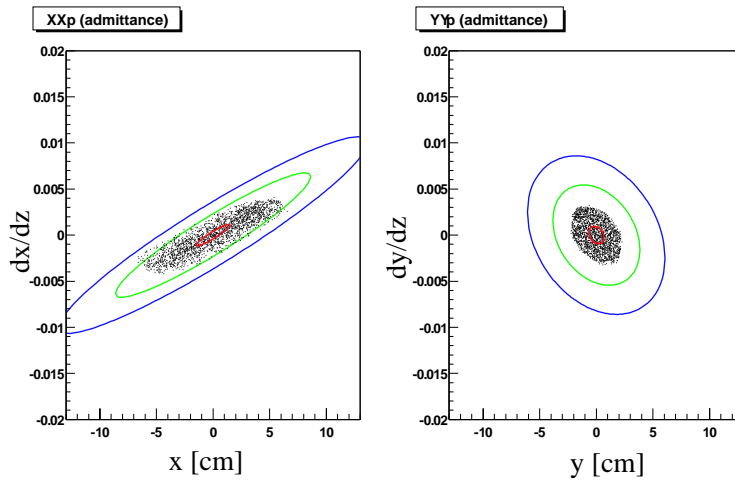


Figure 4.2: The phase space distribution at the extraction point. We generate the beam halo with the parameters of  $\epsilon = 500\pi$  mm·mrad,  $dp/p = 0.02$  (blue line), and the particles passing through the preparation section are plotted with black dots. Red line shows the size of beam core,  $\epsilon = 6\pi$  mm·mrad. Green line indicates the beam size of  $\epsilon = 200\pi$  mm·mrad, which is the assumed beam halo in this study.

## 4.2 Beam Loss Estimation

By using Geant4, the beam loss at each component is estimated. Figure 4.3 shows the energy deposited by the incident protons and shower particles to each component of the beamline. Here, normalization is obtained by assuming that the total beam loss in the preparation section is 750W, which is 0.1% of the designed beam power (Fig.3.1).

In the later section, we show the fraction of the lost beam particles and the energy deposit in the preparation and arc sections (Table 4.1) with the baseline design of collimators described in Section 3.1.1. Though this result may depend on the parameters of the incident beam halo or the alignment error of magnets and so on, in the current study, the total energy deposit in the arc section is estimated to be a few Watts, which satisfies the limitation of beam loss in the arc section.

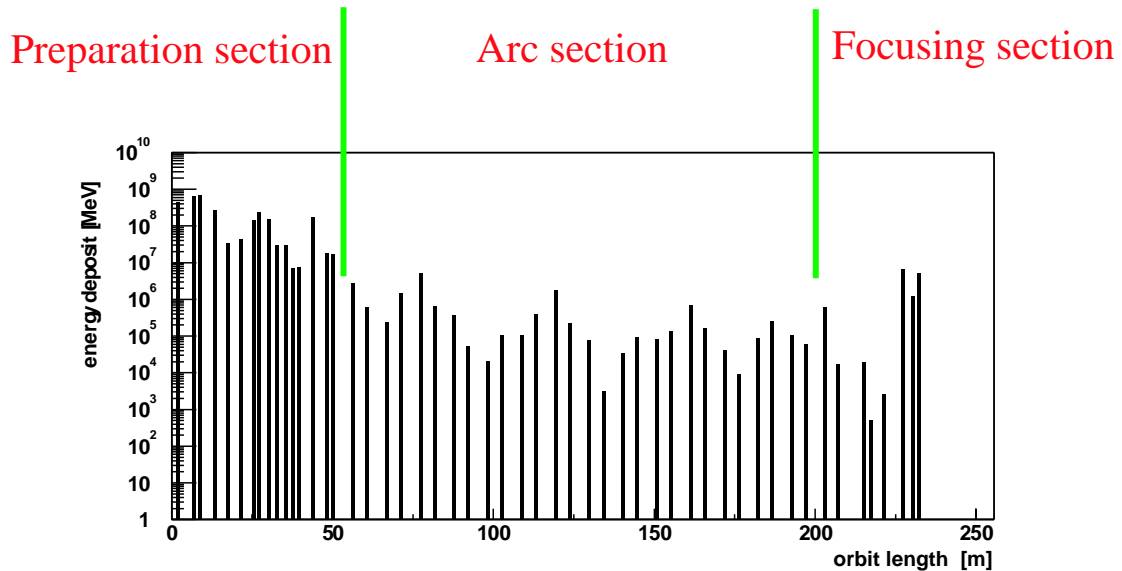


Figure 4.3: The energy dropped by the incident protons and shower particles to each component of the beamline. The horizontal axis is length along the orbit in unit of meter.

### 4.3 Radiation Dose of Magnets in the Preparation Section

The preparation section is designed to accept and transport as much beam as possible from the primary proton beam line keeping a large acceptance of  $\epsilon = 60\pi$  mm · mrad, and to remove as much beam halo outside  $\epsilon = 60\pi$  mm · mrad as possible to protect the superconducting magnets in the arc section from quenching due to the excessive radiation dose. In the current design the beam halo is scraped off by both the (normal conducting) magnets and collimators in the preparation section.

Since the magnets receive considerable amount of radiation, they become activated and could be damaged. Some of them may need to be built radiation resistant using the Mineral Insulation Magnet Cables (MIC) technology. We have estimated the radiation dose of each of 12 magnets in the preparation section with a GEANT-based beam line simulation. We assume all the magnets are made of iron, size of 4 collimators is the baseline design shown in Table 3.1, and we calculate the total annual dose (in units of Gy=Gray=Joule/kg) assuming a total operation time of 4000 hours a year.

The spatial distribution of the energy deposited in the magnet iron is shown in Fig.4.4 for PH1, that is located most upstream. (Note that each of three plots represents the projection of the three dimensional distribution to one of three coordinates.) Figure 4.5 shows the fraction of the energy deposited within 5-cm thick iron around the magnet aperture for each of 12 magnets plus 4 collimators in the preparation section. These indicate that most of the energy is absorbed in the iron within 5 cm from the magnet aperture.

Figure 4.6 shows the total radiation dose a year for each of 12 magnets plus 4 collimators (PC1-4). The dose in Gy is calculated assuming all the energy of lost protons is deposited within 5-cm thick iron around the magnet aperture. It indicates that the first four magnets receive radiation more than the collimators that are installed further downstream.

We have also investigated the radiation dose distribution within the iron. Figure 4.7 shows the total radiation dose a year at the location where the maximum energy loss (joule/cm<sup>3</sup>) occurs.

Requiring that the magnets receiving more than  $10^6$  Gy/year should be

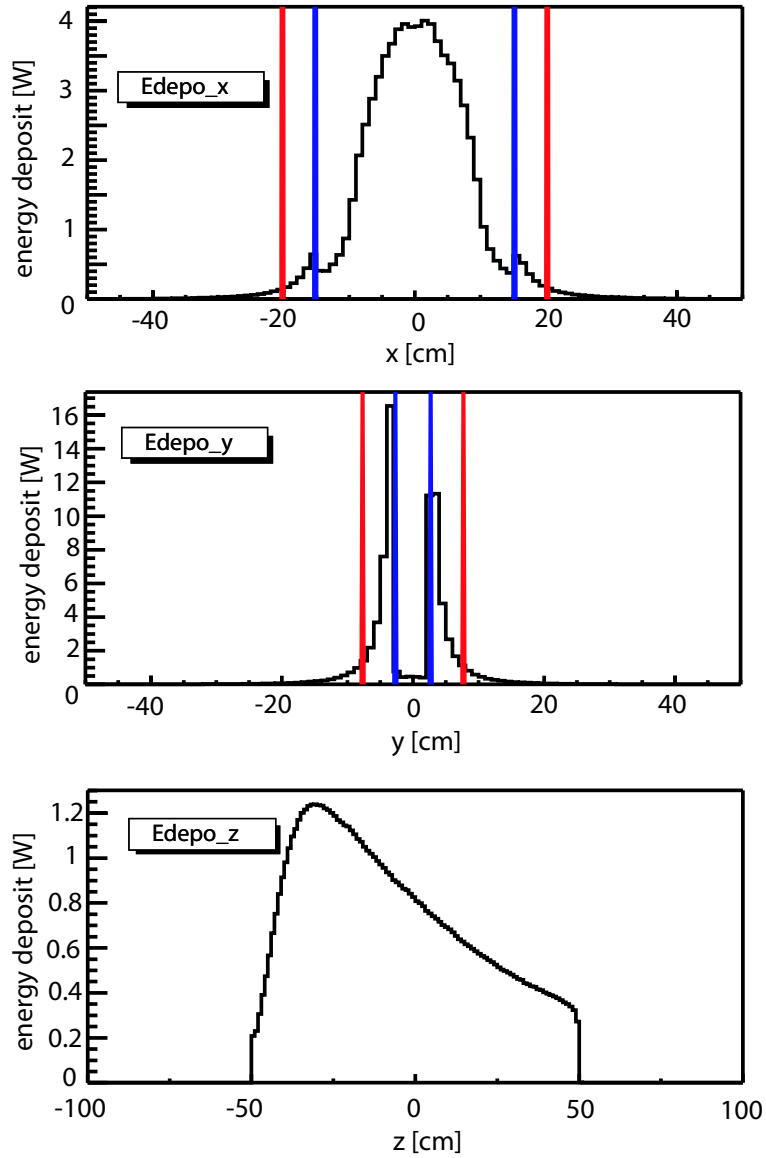


Figure 4.4: The spatial distribution of the energy deposited in the magnet iron for PH1. Each of three plots represents the projection of the three dimensional distribution to one of three coordinates. Up:horizontal, Middle:vertical, Down:direction of the beam axis. Blue line indicates the magnet aperture, and red one indicates 5-cm thick around the aperture.

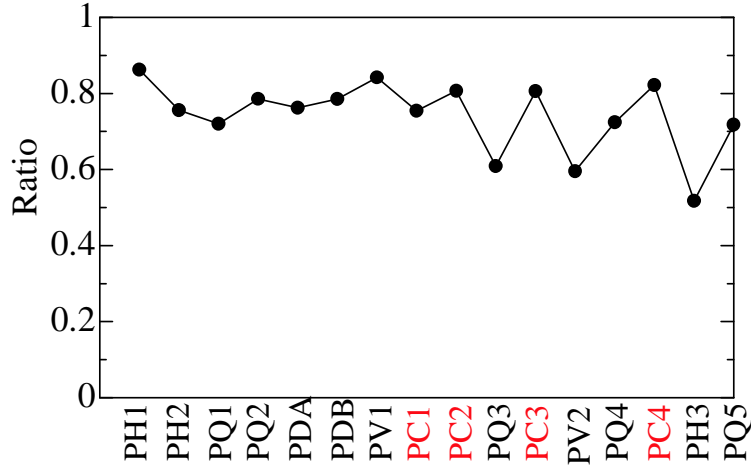


Figure 4.5: The fraction of the energy deposited within 5-cm thick iron around the magnet aperture.

MIC magnets <sup>1</sup>, the results in Figs.4.6 and 4.7 indicate that 4 upstream magnets (PH1, PH2, PQ1 and PQ2) and PV1 need to be built with MIC. This requirement may be relaxed if the magnet coil resides outside of 5-cm thick iron part, and therefore it receives little radiation. Further assessment of the results is under way.

---

<sup>1</sup>The normal conducting magnet is believed to stand up to  $10^8$  Gy. The magnets receiving  $10^6$  Gy/year could function for  $\sim 100$  years.

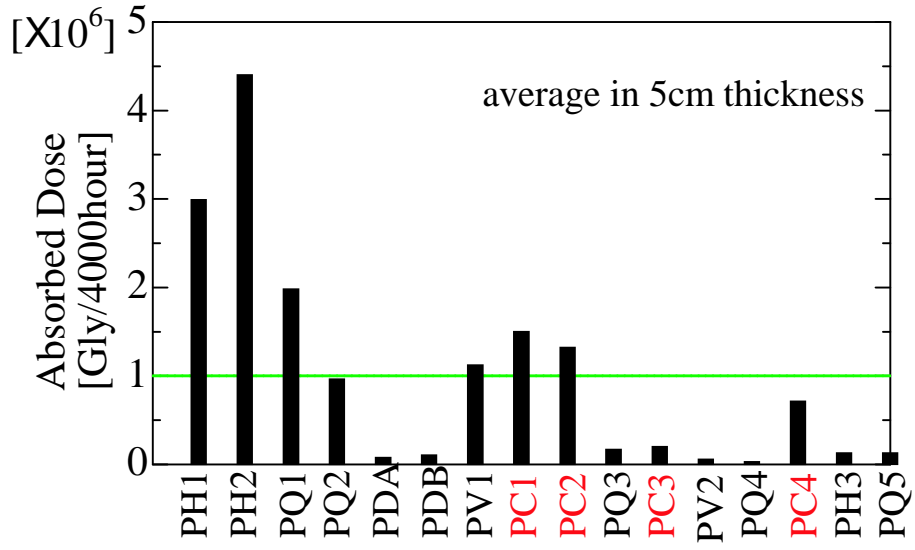


Figure 4.6: The total radiation dose a year calculated assuming all the energy of lost protons is deposited within 5-cm thick iron around the magnet aperture. Green line indicates  $10^6$  Gy/year. Above this line, the magnet is required to be built with MIC.

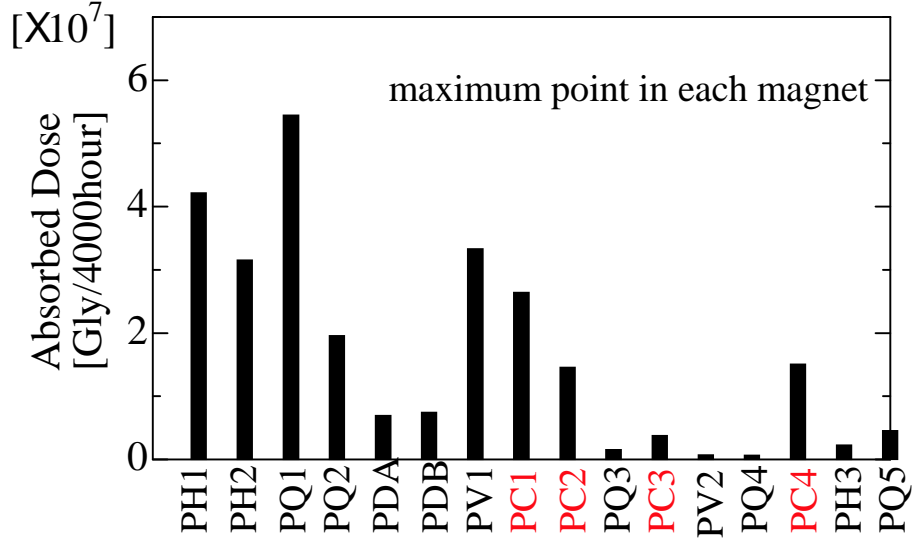


Figure 4.7: The total radiation dose a year at the location where the maximum energy loss ( $\text{joule}/\text{cm}^3$ ) occurs.

## 4.4 Optimization of Design Parameters for Collimators

The major scraping of the beam halo is expected to take place at the first four magnets in the preparation section as shown in the previous section. However, as shown in Table 4.1, if we do not install the collimators at all, the beam loss and energy deposit in the arc section is larger than that with four collimators. The collimators play an important role to further suppress halo-induced background at the arc section.

Due to the space limitation within the preparation section, we have no room to increase the numbers nor change the positions. To optimize the collimator design we have simulated collimators with various dimensions and materials. We summarize the results in the following.

	primary loss [%]		energy deposit [W]	
	Preparation Section	Arc Section	Arc Total	Arc 1st CF magnet
nominal collimators	$88.0 \pm 0.3$	$0.63 \pm 0.03$	2.71	0.47
no collimators	$79.8 \pm 0.3$	$1.38 \pm 0.04$	5.86	1.11

Table 4.1: The fraction of the lost beam particles in the preparation and arc section, and the total energy deposit in the arc section and that in the first superconducting magnet with the baseline collimators (Table 3.1) and without the collimators, respectively.

- Collimator Size and Material : Figure 4.8 shows the shape of the collimators and Table 3.1 lists the nominal dimensions. In order to optimize the collimator design, we vary the material, thickness and length of the collimator and check the energy loss in the arc section as well as in the magnets near the collimators.

Figures 4.9 and 4.10 show the energy deposited in the arc section and that in the nearby magnets, respectively, with three values of the thickness of the collimator wall (1cm, 5 cm and 50 cm) for two materials (iron and tungsten). All results show that the 5 cm thick iron gives nearly identical amount of radiation loss as the 50 cm thick iron. We find no significant difference between iron and tungsten.

Figure 4.11 shows the loss of the number of beam particles and the energy deposit in the arc section for 4 different collimator lengths. Figures 4.12 and 4.13 show the energy deposit in the first superconducting magnet in the arc section and that in the normal conducting magnets near the collimators (in the preparation section), respectively. All results clearly show the background radiation in the arc section and in the nearby magnets highly depends on the length of the collimators. To minimize the energy loss in the arc section, therefore, the collimator should be as long as possible, i.e., collimators should fill up as much drift space of the preparation section as possible. Also long collimators reduce the radiation to the nearby normal conducting magnets. We conclude that the length of the collimator must be maximized.

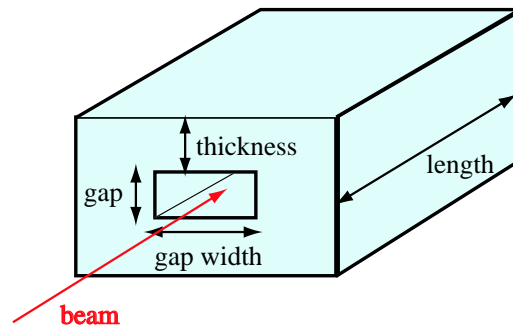


Figure 4.8: Shape of the collimators.

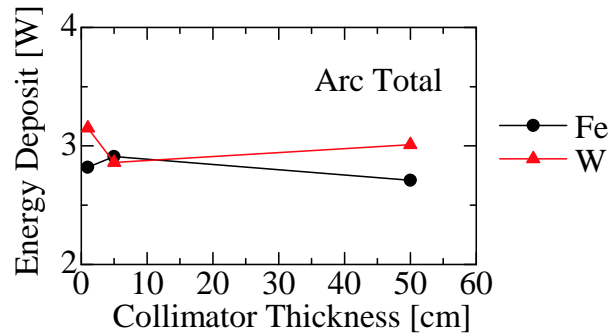


Figure 4.9: The energy deposit in the arc section with three values of the collimator thickness (1cm, 5 cm and 50 cm) for two materials (red:tungsten, black:iron).

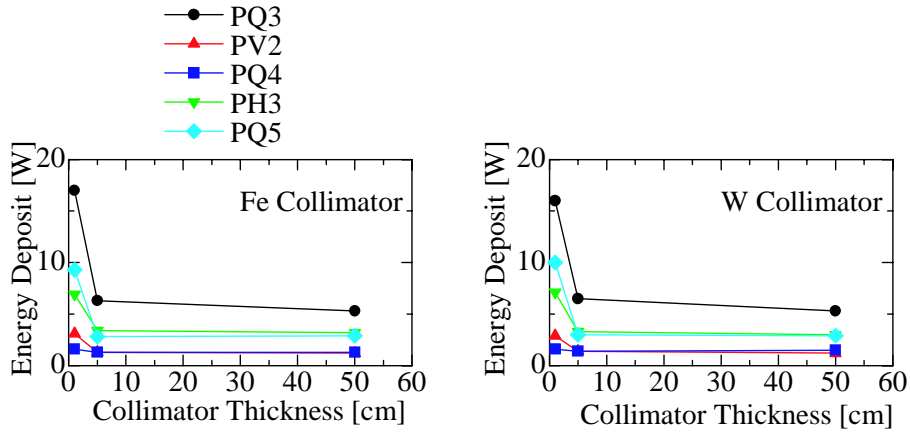


Figure 4.10: The energy deposit in the normal conducting magnets near the collimators for three values of the collimator thickness and for two materials (left:iron, right:tungsten).

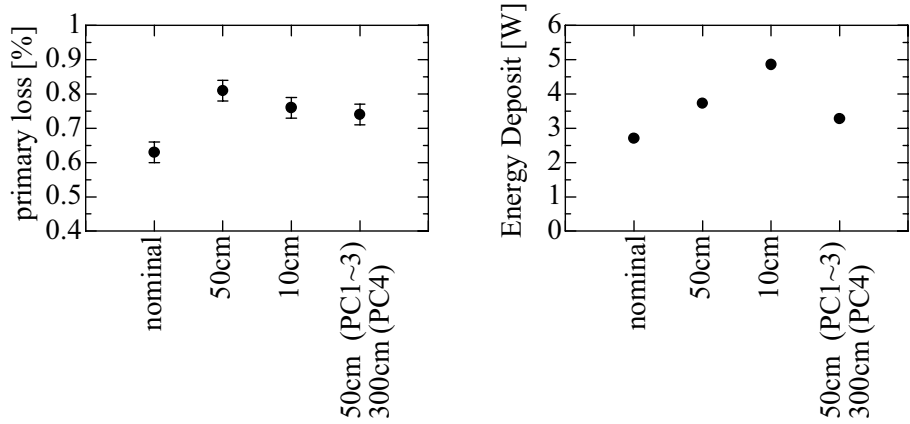


Figure 4.11: The loss of the number of beam particles (left) and the energy deposited in the arc section (right) for 4 different collimator lengths; the length in Table 3.1 (nominal), 50-cm or 10-cm length for all 4 collimators, and 50-cm for PC1,PC2,PC3 and nominal value for PC4.

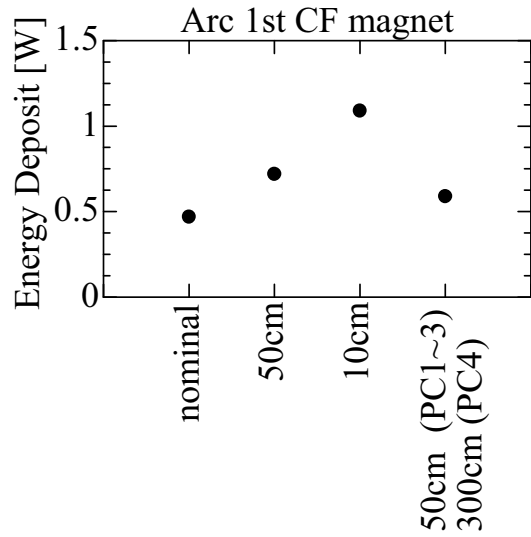


Figure 4.12: The energy deposit in the first superconducting magnet in the arc section for 4 different collimator length.

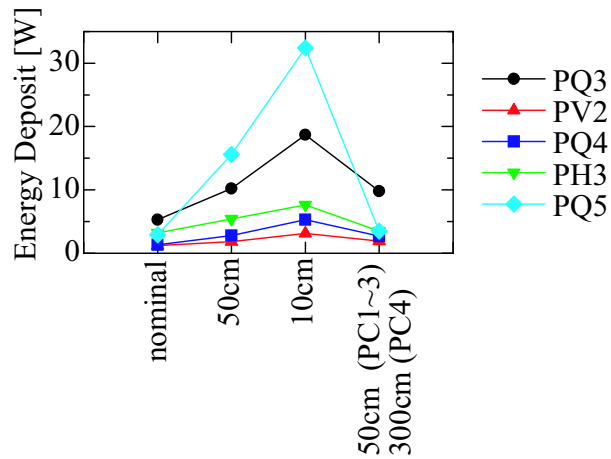


Figure 4.13: The energy deposit in the normal conducting magnets near the collimators (in the preparation section) for 4 different collimator length.

- Collimator Gap Size : In order to estimate the effect of the collimator gap size, we simulate the beam loss with the collimators having the 5% smaller gap area than the default value. These small-gap collimators correspond to the acceptance of  $\epsilon = 55\pi$  mm · mrad instead of the nominal  $60\pi$  mm · mrad. Figure 4.14 shows the energy deposit in each of 12 magnets plus 4 collimators (PC1-4). The effect of the reduced collimator gap size is very small as we expect from the fact that the primary scraping of halo particles happen at the first four magnets. Figure 4.15 shows the loss of the number of beam particles and the energy deposit in the arc section for two sets of collimators with the nominal  $\epsilon = 60\pi$  mm · mrad and  $55\pi$  mm · mrad. The effect of the reduced collimator gap size is also small.

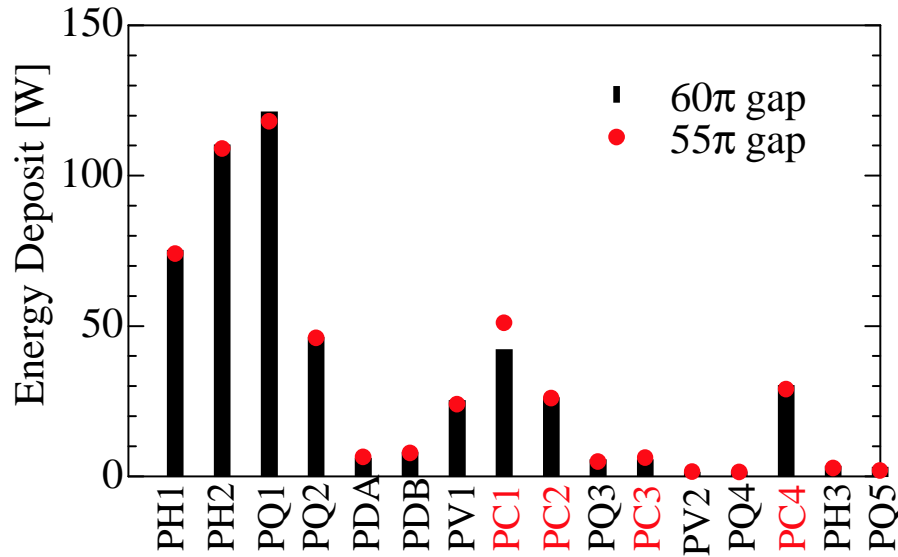


Figure 4.14: The energy deposited in the magnets and collimators (in the preparation section) for two collimator gap size. Black bar: collimator acceptance corresponds to  $\epsilon = 60 [\pi \cdot \text{mm} \cdot \text{mrad}]$ , red point:  $\epsilon = 55 [\pi \cdot \text{mm} \cdot \text{mrad}]$ .

In order to understand the function of the preparation section, we plot, in Fig.4.16, the phase space distributions of the particles that survive the preparation section collimators and, then, become lost from the beam pipe at the arc section. The collimators can scrape off the particles distributed over the larger  $X$  position than the collimator gap size. The particles at PC1,2 and 3 are concentrated around  $X = 0$

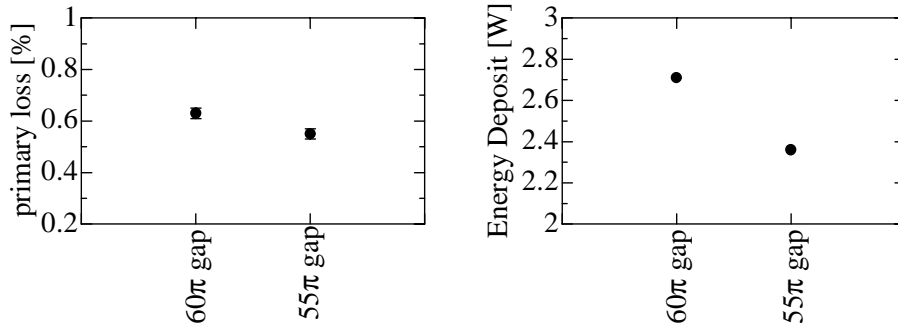


Figure 4.15: The loss of the number of beam particles (left) and the energy deposited in the arc section (right) for two sets of collimators with the nominal  $\epsilon = 60\pi$  mm · mrad and  $55\pi$  mm · mrad, respectively.

and, therefore, it is not effective to further reduce the gap size. The same phase space distributions at the first magnet (PH1) and the exit of the preparation section are shown in Fig.4.17. In these positions, since the particles are distributed relatively outside in the  $X$ -direction, the collimators placed at the two locations would be effective to further remove halo particles.

## 4.5 Radiation Shield at the Exit of the Preparation Section

Halo particles are scraped off in the preparation section and secondary particles are generated in hadron showers. The latter secondary particles could leak into the arc section and induce excessive radiation dose to the superconducting magnets. The shield that fills the entire space between the beam pipe and the tunnel wall, a tunnel filler, at the intersection of the preparation and arc section would be effective to protect the arc section if secondary particles scatter outside the beam pipe. To study the effect of this shield, we estimate the amount of beam loss in the arc section with the 1-meter thick tunnel filler placed at the exit (1m downstream from the last magnet) of the preparation section. We assume the same beam halo as described above (spread uniformly over the phase space of  $\epsilon = 200\pi$  mm · mrad and having the momentum dispersion of  $dp/p = 0.02$ ). We have simulated three different shield materials, concrete, iron and (even) tungsten. Table 4.2 lists the

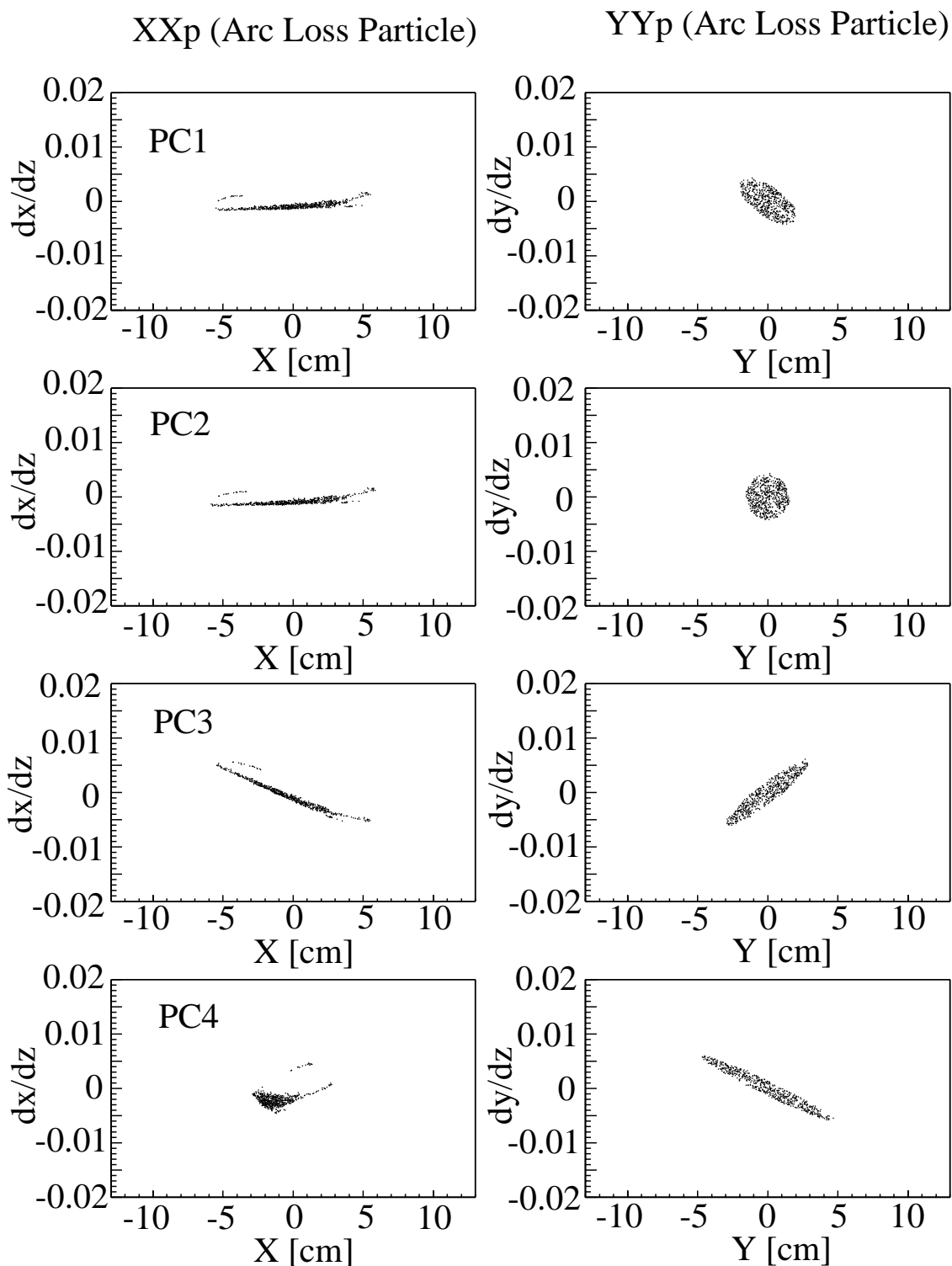


Figure 4.16: The phase space distributions at the collimators of the particles become lost at the arc section. Each row shows the phase space at the entrance of PC1 to PC4, respectively. And left column shows horizontal phase space, and right shows vertical.

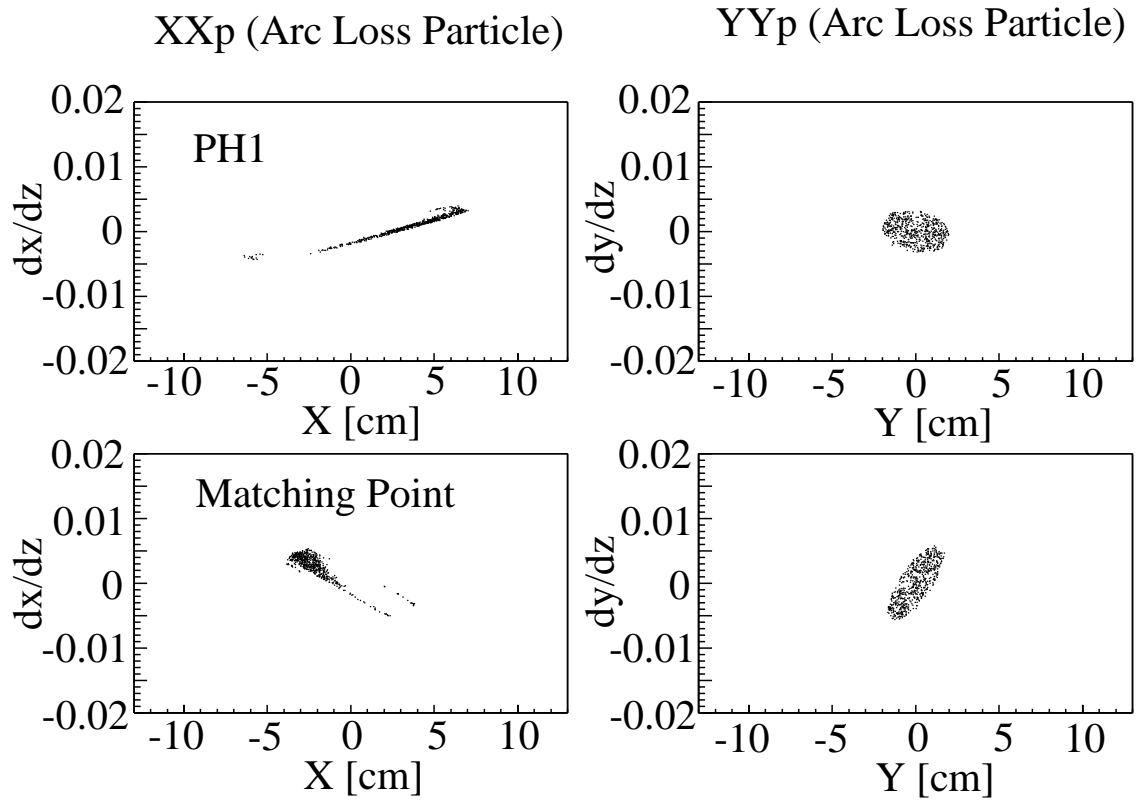


Figure 4.17: The phase space distributions at the PH1 and exit of the preparation section of the particles become lost at the arc section. Upper: at the entrance of PH1, lower: exit of the preparation section.

fraction of the lost beam particles and the energy deposit in the preparation and arc sections without the tunnel filler shield. Note that in this section, the beamline design is old a few. Therefore the beam loss for the baseline design in Table 4.2 is different with Table 4.1. We think it does not influence the conclusion.

Figures 4.18 and 4.19 show the fraction of lost particles and energy deposit, respectively, as a function of the inner diameter of the shield for three materials. It should be noted the largest inner diameter of 100 mm is smaller than the inner diameter ( $\sim 130\text{mm}$ ) of the superconducting magnets of the arc. The results with the diameter of 100 mm are nearly identical with those without the shield. This strongly suggests that most of secondary particles leaking into the arc section are coming through the beam pipe and hit the arc section magnets from inside. Making the inner diameter of the shield smaller helps to reduce the fraction of lost particles in the arc section as shown in Fig.4.18 (right). This, however, increases the energy deposit in the superconducting magnet immediately downstream the shield (Fig.4.19 (right)) due to secondary shower particles generated at the shield. Consequently the total heat generated in the arc section for the smaller diameter shield is more than that for no shield. The current simulation study does not support the idea of having a tunnel filler shield at the exit of the preparation section. Further optimization is under way.

	primary loss [%]		energy deposit [W]	
	Preparation Section	Arc Section	Arc Total	Arc 1st CF magnet
No Shield	$84.9 \pm 0.3$	$0.86 \pm 0.03$	3.66	0.35

Table 4.2: The fraction of the lost beam particles in the preparation and arc sections, and the energy deposited in the arc total and first superconducting magnet, without the tunnel filler shield.

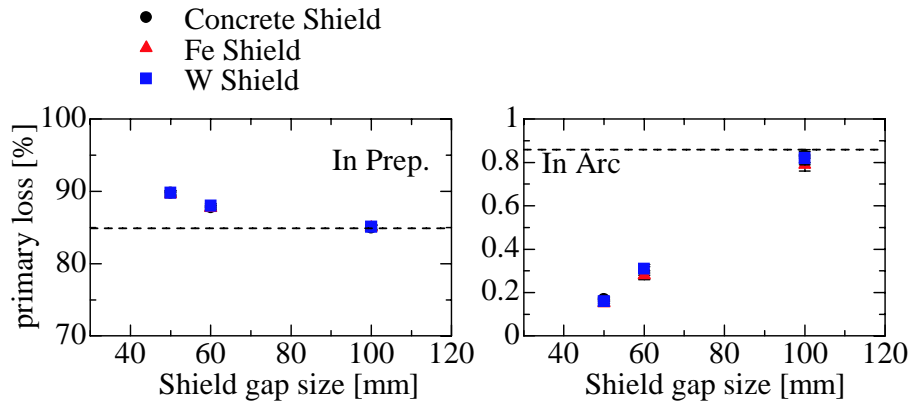


Figure 4.18: The fraction of lost particles in the preparation section (left) and arc section (right) for three materials, respectively, as a function of the inner diameter of the shield. Dashed line indicates the values without the tunnel filler shield.

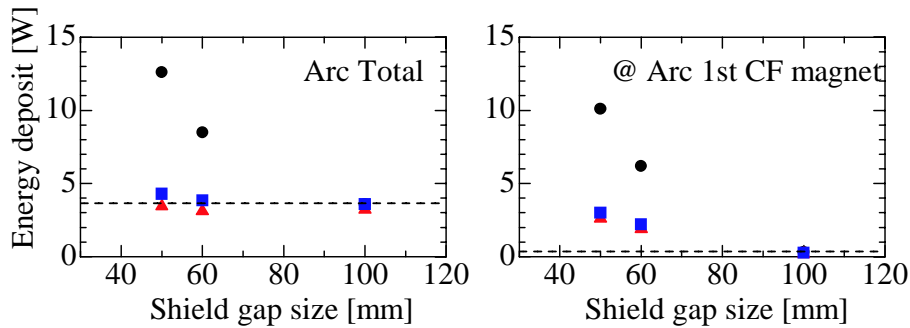


Figure 4.19: The fraction of energy deposit in the arc (left) and superconducting magnet immediately downstream the shield (right), as a function of the inner diameter of the shield. Dashed line indicates the values without the tunnel filler shield.

## 4.6 Summary

In the J-PARC neutrino beamline, the beam loss in the arc section is restricted to protect the superconducting magnets from quenching. To estimate the beam loss generated by the beam halo, we have carried out the beamline simulation based on Geant4.

In the current study, the total energy deposit in the arc section is as small as a few Watts, though this result may depend on the parameters of the incident beam halo, or the alignment errors of magnets and so on.

With the beamline simulation, we have also optimized the design parameters of some components. About the collimators, the result shows that the 5 cm thick iron gives nearly identical amount of radiation loss as the 50 cm thick iron, while the radiation loss clearly depends on the length of the collimators. We think the 5cm is thick enough, but length of the collimators must be maximized. And the effect of the 5% smaller collimator gap size is small, because in the preparation section, the major scraping of the beam halo takes place at the first four normal conducting magnets.

The simulation result also shows that in the preparation section, the radiation dose is large at these four upstream magnets and one steering magnet (named PV1). They may need to be built with the radiation resistant MIC magnets.

We have also estimated the effect of the radiation shield at the exit of the preparation section. The result of current simulation does not favor the radiation shield at the exit of the preparation section, because the shield generates the secondary shower particles, which hit, in particular, the superconducting magnet immediately downstream the shield.

# Chapter 5

## R&D of the Segmented Secondary Emission Monitor

It is important in the J-PARC neutrino beamline to control the proton beam using various beam monitors as described in the Section 3.2, to suppress beam loss as much as possible, to keep generated neutrino beam stable and to control it precisely. The R&D of several kinds of beam monitors has started. The profile monitor is one of such monitors. For profile monitors, the following requirements are considered.

- Minimum amount of material in the beamline, to reduce the beam loss.
- Long lifetime in the high radiation environment, and easy maintenance.
- Wide dynamic range to operate from the initial low intensity to the full design intensity. ( $10^{12} \sim 10^{14}$  protons/pulse.)
- Profile measurement resolution should be  $1 \sim 2$  mm.
- The dimensions of the monitor are restricted by the space between the magnets and other beam line elements.

Two candidates for the profile monitor in the J-PARC neutrino beamline are studied. One is a monitor utilizing the phenomenon of secondary emission : SSEM (Segmented Secondary Emission Monitor), and the other is based on the ionization of the residual gas : RGBPM (Residual Gas Beam Profile Monitor). In this section, we describe the current status of the R&D of SSEM.

## 5.1 Principle of the Secondary Emission Monitor

Figure 5.1 shows a schematic view of SSEM. This monitor consists of anode and cathode electrodes made of thin metal foils. The secondary electrons are emitted, if the incident proton beam traverses these electrodes. The number of the secondary electrons is proportional to the intensity of the incident proton beam. Anode electrodes absorb these secondary electrons. Signals are read out from cathode electrodes as pulses with positive polarity. The segmentation of cathode electrodes using strips or wires enables us to measure the beam profile.

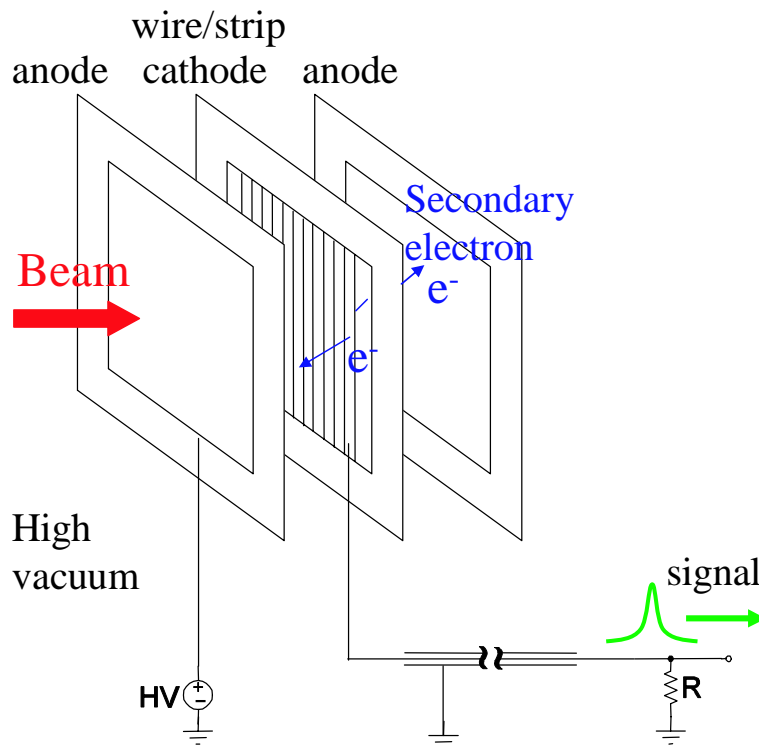


Figure 5.1: a schematic view of SSEM.

## Estimation of the number of secondary electrons

The number of secondary electrons emitted from cathode electrodes can be estimated using the empirically obtained secondary emission efficiencies. SEMs with a cathode electrode made of aluminum are used in many experiments (see, for example, [8],[9],[10],[11],[12]). In these experiments, the secondary emission efficiency from aluminum cathode electrodes is reported to be several % for incident charged particles, which are protons or electrons in the energy range of MeV to GeV.

We use the value of 2.1% for each side of aluminum electrodes as the secondary emission efficiency [13]. The cathode electrode is assumed to be a single foil made of aluminum, which has enough dimensions to cover the whole beam. The number of secondary electrons is given by

$$Q_{SEC} = 0.021 * 2 * e * Int \text{ [C/pulse]}, \quad (5.1)$$

where  $e$  is the electron charge magnitude, and  $Int$  is the intensity of the incident proton beam given as protons per pulse.

Most of the secondary electrons have low energies  $\sim 20$  eV. These low energy electrons can escape from the maximum depth about 10nm below the surface. Therefore the number of secondary electrons does not depend on the thickness of electrodes, rather it depends on the surface condition of the electrodes [14, 15].

The surface condition of the electrodes is thought to influence the long term stability of the SSEM performance. In some experiments, the reduction of secondary emission efficiency is observed, in particular, at the position of electrodes where the incident proton beam irradiates locally ( [8], [9], [16], [17]). These long term instability is thought to be due to the reduction of oxide layer or contamination by carbon compound (like CO gas adsorption) on the surface of electrodes. In these experiments, for the aluminum cathode electrodes, the secondary emission efficiency reduces 0.4  $\sim$  2 % per  $10^{18}$  incident protons/cm<sup>2</sup>. According to ref.[17], for titanium this change of secondary emission efficiency in the long term is smaller than the change for aluminum or gold.

The opposite behavior is observed in the experiment using the low energy incident electron beam (up to several keV). In this experiment, the metal samples are made in the high vacuum environment by the sputtering method. Their secondary emission efficiencies increase after the hours of exposure to

air by the contamination of their surfaces ([18]).

### Estimation of the vacuum for the SSEM

Because the electric field setup of the SSEM is nearly identical to that of the ionization chamber, the SSEM could produce signal due to ionization of the residual gas in addition to the secondary emission signal. In the following we estimate the ionization signal (relative to the secondary emission signal) as a function of the vacuum.

In this estimation, the main component of the residual gas is assumed to be nitrogen. For the nitrogen gas, we assume that the density is  $d = 1.25 \times 10^{-3}$  [g/cm<sup>3</sup>],  $dE/dx$  is  $1.825 \times 10^6$  [eV/g/cm<sup>2</sup>], and the ionization energy is  $W = 35$  [eV], respectively. The length of the volume containing the residual gas is assumed to be  $l = 1.5$ cm, which is the distance between the two anode electrodes.

The energy dropped by one incident proton is

$$dE = \frac{dE}{dx} * l * d * \frac{P}{760} \text{ [eV]},$$

where  $P$  is the pressure of the nitrogen gas in Torr. Therefore the number of ion pairs generated by the incident proton beam with the intensity of  $Int$  [protons/pulse] is

$$N_{pair} = \frac{dE}{W} * Int \text{ [pairs/pulse]}.$$

The amount of the charge of the ionized electrons or ions is

$$Q_{IC} = N_{pair} * e \text{ [C/pulse]}.$$

On the other hand, we calculate the amount of the charge of secondary emission using Eq.5.1. The ratio of these estimated values is approximately

$$\frac{Q_{IC}}{Q_{SEC}} \sim 3.1 * P. \tag{5.2}$$

The Eq.5.2 is plotted in Fig.5.2. The above estimate shows that the signal due to ionization is negligible for the beam line vacuum of  $10^{-6}$  Torr, the current design value.

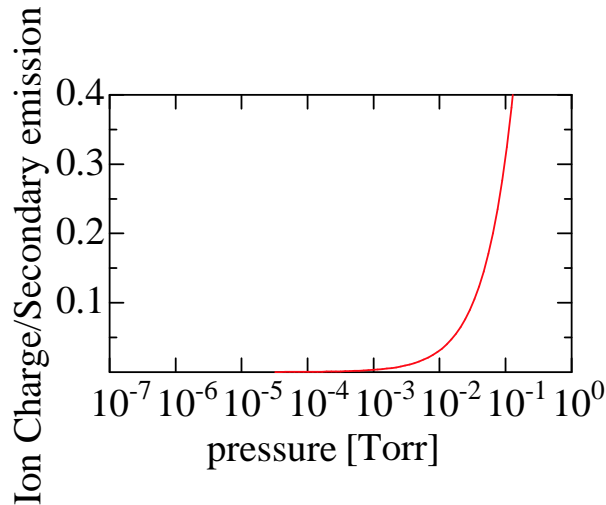


Figure 5.2: the ratio of the number of secondary electrons and ion pairs

## 5.2 The requirements for the design of the SSEM

In order to use SSEM in the J-PARC neutrino beamline, where high intensity proton beam passing through, there are some requirements:

- The amount of the electrode material must be minimized. (a few  $10^{-5}$  interaction length)
- The secondary emission efficiency must be as high as possible.
- The electrodes must stand heating due to the beam.
- The SSEM must not disturb the beam except for beam tuning, (and therefore, the SSEM must be movable.)
- The SSEM must fit in the limited space between the beam line elements.

In this section, we discuss these requirements in detail.

### The amount of material and the design of electrodes

SSEM inevitably induces the beam loss. Therefore electrodes must be as thin as possible. Table 5.1 shows the thickness equivalent to the  $10^{-5}$  interaction

length ( $\lambda_{\text{int}}$ ) for typical metals. Because the full beam power in J-PARC 50GeV is very large (750kW), even a very thin metal electrode could produce sizeable beam loss (e.g. 7.5W for a material of  $10^{-5}$  interaction length). In the arc section, the maximum allowable beam loss is assumed to be less than 1 W/m line loss. In terms of point loss, thickness of radiation shield in arc is calculated by assuming 10W/point point loss [6].

If we measure the both horizontal and vertical profiles at one position, two cathodes and three anodes are necessary. For example, the total material become about  $5 \times 10^{-5} \lambda_{\text{int}}$  if we use the five titanium foils with the thickness of 2.75  $\mu\text{m}$ . This beam loss is 37.5W/point, which is larger than the assumed point loss.

To solve this problem, we consider to make electrodes with proper material and shape, and to get the SSEM away from the beamline with the movable structure, at usual operations, except for the time of beam tuning.

Material	Thickness [ $\mu\text{m}$ ] equivalent to $10^{-5} \lambda_{\text{int}}$
Al	3.94
Ti	2.75
Fe	1.68
Cu	1.51
W	0.96

Table 5.1: Thickness of materials equivalent to  $10^{-5} \lambda_{\text{int}}$ .  $\lambda_{\text{int}}$  is an interaction length.

To reduce the effective amount of material, two methods are considered: One is to place the strips or wires sparsely to reduce the area of electrodes. However, the distance from the center of a cathode to neighboring one is limited to be 1  $\sim$  2mm at the maximum taking into account the minimum beam size. Considering this limitation, we discuss the issues of strips and wires, respectively.

- Strips

To reduce the area of electrode, the strips should be as narrow as possible. However, if the strips get narrower, signals from them also become smaller. If we consider the estimation of signal charge described later, the width of strips should be at least  $\sim$  1mm. With the 1mm

wide strips placed at the intervals of 2mm, the amount of material is the half of the foil electrode.

- Wires

If we use the wires, the fraction of the protons passing through them can be small. However, the amount of signal charge from wires is also small. For example, we compare the wire with the diameter of  $100\mu\text{m}$  with a 1mm wide and  $7.5\mu\text{m}$  thick strip. They has almost the same amount of material, while the amount of signal from the wire is about  $1/7$  of that from the strip. It is too small for the beam intensity of  $10^{12}$  protons/pulse. Therefore strips are more preferable to wires.

The other method is to make a hole in each anode electrode to make the beam pass through this hole. Or we may be able to remove one or both of the anode electrodes in the both side of cathode electrode. We plan to investigate whether SSEM can work properly with anode electrode with a hole, or even without an anode electrode.

### **The lifetime of the monitor**

Concerning the lifetime of SSEM, one issue is the change of the secondary emission efficiency in the long term. As described in the previous section, the change of the secondary emission efficiency could become a few % for each  $10^{18}$  incident protons/cm<sup>2</sup>.

This corresponds to the order of  $10^5$  pulses for the beam with 2cm diameter, roughly 100 hours in the J-PARC neutrino beamline. We use SSEM only during the time of beam tuning. Therefore the change in the efficiency will be smaller than this estimation.

### **The expected signal**

We estimate the amount of expected signal charge for the J-PARC proton beam in the following. The cathode electrodes are assumed to consist of aluminum. For the other materials, we can get their secondary emission efficiencies in [14] for example.

The signal charge is calculated using Eq.5.1 for a foil electrode which covers the whole beam. For the segmented cathode electrodes, like strips and wires, we estimate their signal charge considering the number of incident protons

and the shape of the electrode. In the following, we assume the width of strips is  $w$  and the radius of wires is  $r$ . We also assume the beam shape is circle, the radius of beam is  $R$ , and protons are distributed uniformly in it.

- If the strip or wire is in the center of the beam, the number of incident protons is roughly  $\frac{2wR}{\pi R^2}$  and  $\frac{4rR}{\pi R^2}$  of the whole beam, respectively.
- If the diameter of a wire is the same as the width of a strip ( $2r = w$ ), the number of incident protons is identical. However, the surface area of the wire is  $\sim \pi/2$  times larger than that of the strip. We assume this increase of the surface area causes the increase of secondary emission, since the low energy secondary electrons are able to escape from near surface.

Using the signal charge from the foil electrode ( $Q_{SEC}$ ), we can describe the signal charge from the central strip ( $Q_{strip}$ ) and wire ( $Q_{wire}$ ) as follows:

$$Q_{strip} = \frac{2wR}{\pi R^2} * Q_{SEC}, \quad (5.3)$$

$$Q_{wire} = \frac{4rR}{\pi R^2} * \frac{\pi}{2} * Q_{SEC}. \quad (5.4)$$

The result is shown in Table 5.2, where we assume  $w = 1\text{mm}$ ,  $r = 50 \mu\text{m}$ , and  $R = 1\text{cm}$ , respectively.

The signal is large enough for the beam intensity of  $3.3 \times 10^{14}$  protons/pulse. Considering the bunch width of about 50 nsec. and structure of 8 bunches/pulse at J-PARC, signals of 1nC/pulse correspond to about 2.5mA/bunch. The signal of wires for the  $10^{12}$  protons/pulse seems to be small.

Note that if we assume the shape of the beam as a Gaussian distribution with two sigma equal to radius of uniform beam,  $R$ , the signal from a central strip or wire becomes  $\sqrt{\frac{\pi}{2}}$  times larger than that for the uniform distribution beam.

## Heating of electrodes

The electrodes must be resistant to heating due to the incident proton beam. We estimate the degree of temperature rise of the electrode, assuming that the shape of the electrode is the strip, the thickness of the electrode is uniform. We assume that the time development of the electrode temperature

Material	signal charge [nC/pulse]					
	$3.3 \times 10^{14}$ [protons/pulse]			$1.0 \times 10^{12}$ [protons/pulse]		
	foil	strip	wire	foil	strip	wire
Al	2200	140	22	6.7	0.42	0.067

Table 5.2: The amount of expected signal charge: the beam shape is assumed to be circle, uniform distribution with the radius of 1cm. The size of strip and wire are 1mm full width and 100  $\mu\text{m}$  diameter, respectively.

becomes as shown in Fig.5.3 schematically. The temperature will rise sharply when a beam transverses the electrode, and will cool down before the next beam pulse to some extent.

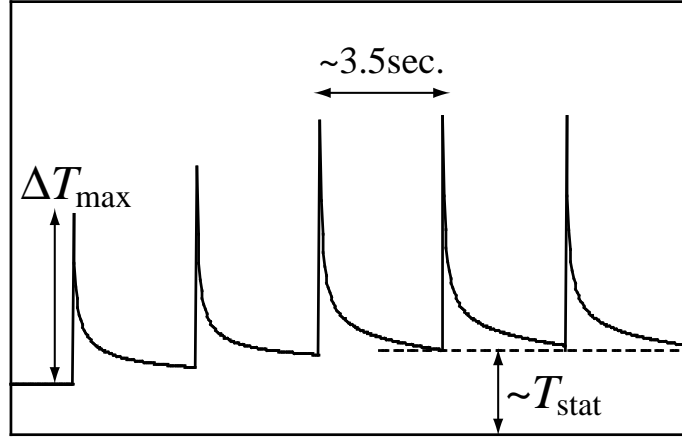


Figure 5.3: Temperature of the electrode versus time.

At first, We estimate the degree of temperature rise due to one incident beam pulse ( $= \Delta T_{\text{max}}$ ). The energy deposit to an electrode by one incident proton is

$$\Delta E = \frac{dE}{dx} * d * \rho,$$

where  $d$  is the thickness of electrode and  $\rho$  is its density. The distribution of heat deposited to electrode is

$$Q(x, y) = \frac{\Delta E * e * 10^6}{J_{\text{cal}}} * f(x, y) [\text{cal}],$$

where  $f(x, y)$  is the distribution function of protons and  $J_{cal}$  is the mechanical equivalent of heat. When the beam hit electrodes, the degree of temperature rise is

$$\begin{aligned}\Delta T &= \frac{Q(x, y)}{\rho dc} \\ &= \frac{\frac{dE}{dx} * e * 10^6}{cJ_{cal}} * f(x, y)\end{aligned}$$

at the each position of electrode.  $c$  is the specific heat. This indicates that the degree of temperature rise does not depend on the thickness of the electrode. The distribution of protons,  $f(x, y)$ , can not be predicted clearly. Here we assume a Gaussian distribution,

$$f(x, y) = \frac{Int}{2\pi\sigma_x\sigma_y} e^{-\left(\frac{x^2}{2\sigma_x^2} + \frac{y^2}{2\sigma_y^2}\right)},$$

where  $Int$  is the intensity of the proton beam in the unit of protons/pulse,  $\sigma_x$  and  $\sigma_y$  are the beam sizes in horizontal and vertical directions, respectively. In this case the maximum temperature rise is described as

$$\Delta T_{max} = \frac{\frac{dE}{dx} * e * 10^6}{cJ_{cal}} * \frac{Int}{2\pi\sigma_x\sigma_y}$$

at the center position of the incident beam. This temperature rise depends on the beam size at the position of the monitor.

The minimum beam size in the positions of the SSEM in the J-PARC neutrino beamline is about 7mm in both horizontal and vertical directions from optics parameters. The  $\sqrt{\beta}$  at the drift space between the superconducting magnets is  $\sim 2.8$  [ $\sqrt{\text{m}}$ ] from Fig.3.3, then the beam size calculated with  $\sqrt{\beta\epsilon'}^1$  is  $\sim 7\text{mm}$  for the emittance of  $6\pi$  [ $\text{mm} \cdot \text{mrad}$ ]. In the practical beam, it is possible that the beam distribution is not Gaussian and that this calculated beam size is not the  $1\sigma$  of the distribution. To estimate the temperature rise conservatively, we assume that this beam size is  $2\sigma$  of the Gaussian distribution.

In Table 5.3, the maximum temperature rise due to one incident beam pulse

---

<sup>1</sup>The emittance of  $6\pi$  [ $\text{mm} \cdot \text{mrad}$ ] in J-PARC means the area of the phase space ellipse. Here we use the notation of  $\epsilon'$  to stand for the another description of the emittance, with which the area of the phase space ellipse can be described as  $\epsilon'\pi$ .

is shown, where we assume that  $\frac{dE}{dx} = 2[\text{MeV}/(\text{g}/\text{cm}^2)]$ ,  $Int = 3.3 \times 10^{14}$  protons/pulse.

Material	specific heat [ cal/g/K ]	thermal conductivity [ cal/cm/K/s ]	density [ g/cm <sup>3</sup> ]	$\Delta T_{max}$ [ K ]
Al	0.215	0.53	2.70	162
Ti	0.126	0.052	4.54	276
Fe	0.11	0.18	7.87	316
Ni	0.107	0.216	8.89	325
Cu	0.092	0.94	8.96	378
Ag	0.057	1.02	10.5	610
W	0.032	0.48	19.3	1087

Table 5.3: Estimated temperature rise due to one beam pulse, as well as the used parameters for the calculation.

In the J-PARC neutrino beamline, the repetition rate of the beam pulse is about 3.5 seconds. We estimate whether this temperature rise cools down before the next beam pulse. Two cooling mechanisms are considered, the thermal conduction and thermal radiation. We will need the numerical computation to estimate the time development of the temperature by the thermal radiation, or to estimate the effect of the thermal conduction and radiation simultaneously. In the following, therefore, we estimate the effect of the thermal conduction and radiation separately.

If we consider the thermal conduction, the time dependence of the temperature rise is calculated from the equation:

$$\frac{1}{\alpha} \frac{\partial T}{\partial t} = \frac{\partial^2 T}{\partial x^2},$$

where  $\alpha = \frac{k}{\rho c}$  and  $k$  is the thermal conductivity. The time dependence of the temperature with the Gaussian distribution is obtained by solving this equation under the boundary condition of  $T(x, t) \rightarrow 0$  ( $x \rightarrow \pm\infty$ ). Figure 5.4 shows the temperature distribution for each material at the three seconds after a 1st beam pulse. The temperature rise is not cooled in three seconds by the thermal conduction. The heating due to the incident beam will be

accumulated.

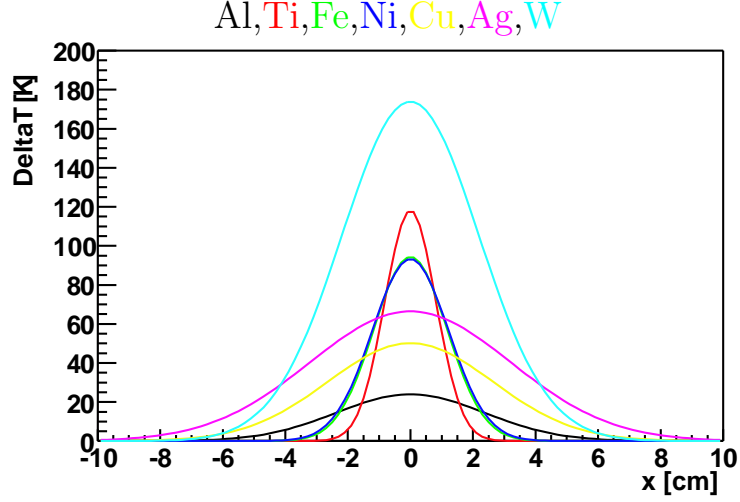


Figure 5.4: The temperature distribution at the three seconds after a beam pulse calculated by thermal conduction only.

To estimate the equilibrium temperature, we roughly estimate the temperature where the input heat from the beam and the output heat by the thermal radiation becomes identical ( $\sim T_{stat}$ ). In the stationary state, for a strip placed at the center of the beam, the amount of the input heat due to the incident beam is described as,

$$q = \int_{-\infty}^{\infty} Q(x, 0) dx \times \frac{w}{3} \quad (5.5)$$

$$= \frac{\text{Int} \frac{dE}{dx} \rho e d w * 10^6}{3\sqrt{2}\pi\sigma_y J_{cal}} \text{ [cal/sec]}, \quad (5.6)$$

where  $w$  is the width of strips, and the heat from one pulse is divided by the repetition rate,  $\sim 3$  sec.

About thermal radiation, we use the assumption that the heat transfer is described as,

$$q_{emit} = \epsilon\sigma(T^4 - T_0^4) \times 2wl,$$

where  $\epsilon$  is the emissivity,  $\sigma$  is the Stefan-Boltzmann constant,  $T_0$  is the surrounding temperature, and  $l$  is the length of the radiation area in strips. We

assume that  $\epsilon = 0.1$  and  $0.01$ ,  $T_0 = 300$  K,  $l = 10$ cm,  $d = 10$   $\mu$ m, and  $w = 1$ mm. In Table 5.4, we show the estimated equilibrium temperature. It indicates that the equilibrium temperature depends on the assumption of the parameters. We may need further study to confirm these results.

Material	$T_{stat}$ [K] from thermal radiation	
	$\epsilon = 0.1$	$\epsilon = 0.01$
Al	365	568
Ti	394	641
Fe	436	732
Ni	446	754
Cu	447	755
Ag	461	785
W	526	912

Table 5.4: The estimated temperature in the stationary state from thermal radiation.

## 5.3 Beam Test at the K2K Neutrino Beamline

We have carried out the beam test at the K2K neutrino beamline twice. The purpose of the 1st beam test is to check the basic performance of SSEM and to compare the several cathode materials. In the 2nd beam test, with the titanium strips as the fine segmented cathode electrodes, we have tested to measure the beam profile.

### 5.3.1 The 1st beam test

#### Design and setup

In this beam test, as the cathode materials, we use five metals shown in Table 5.5 and Fig.5.5. We estimate the amount of signal charge for each cathode metal (Table 5.5). For aluminum, we calculate the amount of signal charge from Eq.5.1 with the assumption that the beam intensity is  $6 \times 10^{12}$  [protons/pulse] and that the shape of cathode electrode is a foil which has enough size to cover the whole beam. For the other cathode materials, we obtain the amount of signal charge from the ratio to aluminum with the ratio of the secondary emission efficiencies given in ref.[14] as a result of 70 MeV electron beam experiment at SLAC.

We require the signals in the order of several nC per pulse from each channel. The repetition rate of the proton beam is 2.2 seconds in the K2K neutrino beamline. The width of one pulse is 1.1  $\mu$ sec. One pulse consists of 9 bunches. If the intensity is unchanged among 9 bunches, the signal charge of several nC per pulse corresponds to signal current in the order of several mA per bunch. We can expect the signal pulse height of more than 100 mV with the 50  $\Omega$  termination oscilloscope. It seems large enough to check the basic response of SSEM.

The beam size at the position of this monitor is about 4cm long vertically and 2cm long horizontally. We set the width of cathode strips to 1.5cm, to require the enough signal charge. The gap size between the strips is 3 mm. We placed them on the base plate, to measure the vertical profile (Fig.5.6). Anode electrodes consist of 7  $\mu$ m thick aluminum foils. These cathode and anode electrodes are placed alternatively at intervals of 7mm. We put the 5

cathode materials in the order listed in Table 5.5 from the upstream of the beamline.

Material	thickness [ $\mu\text{m}$ ]	material size interaction length [ $10^{-5}\lambda_{\text{int}}$ ]	signal charge [nC/pulse/foil]
Al	7	1.78	40
Cu	10	6.62	36
Ti	20	7.27	14
Cu-Be	50	33.1 (assumed pure Cu)	No data for estimation
W	50	52.1	36

Table 5.5: Cathode materials for the 1st beam test.

This monitor is placed before the 1st dump at the K2K neutrino beamline (Fig.5.7). The distance from 1st dump to read-out system is about 150m. We use the shielded twisted pair cables for signal read-out. In this 1st beam test, we check the signal with oscilloscope (50  $\Omega$  termination), and study the basic response of SSEM.

To check the vacuum in SSEM, we use the voltage applied to the ion pump. It depends on the vacuum in SSEM as shown in Fig.5.8, which has been measured before the installation of SSEM to the beamline. Though this is not the direct measurement of the vacuum, we consider the ion pump applied voltage information is useful to know the vacuum condition. To confirm, we also carry out another check with the same type of ion pump and another gauge. The ion pump voltage about 2kV and 4kV corresponds to about  $10^{-4}$  and  $10^{-6}$  Torr, respectively.

## Materials of cathode



**W   Cu-Be   Ti   Cu   Al**

Figure 5.5: Cathode electrodes for the 1st beam test. The width of strips is 1.5cm.

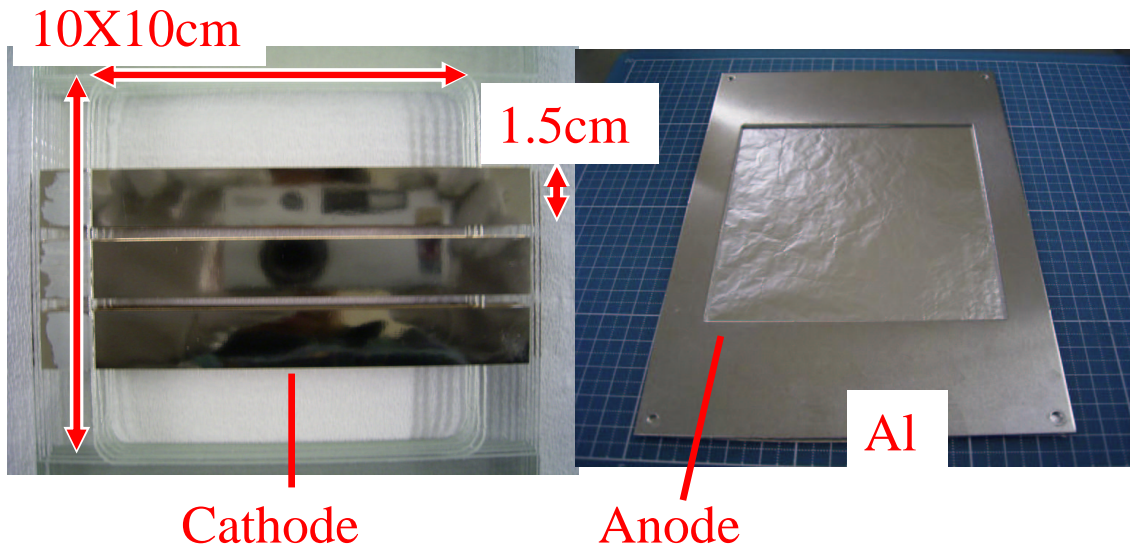


Figure 5.6: Cathode and anode electrodes for the 1st beam test. Strips are placed on the glass base plate as a cathode electrode. The gap size between the strips is 3mm wide. Anode electrodes are made of aluminum foils and are placed on the aluminum base plate.

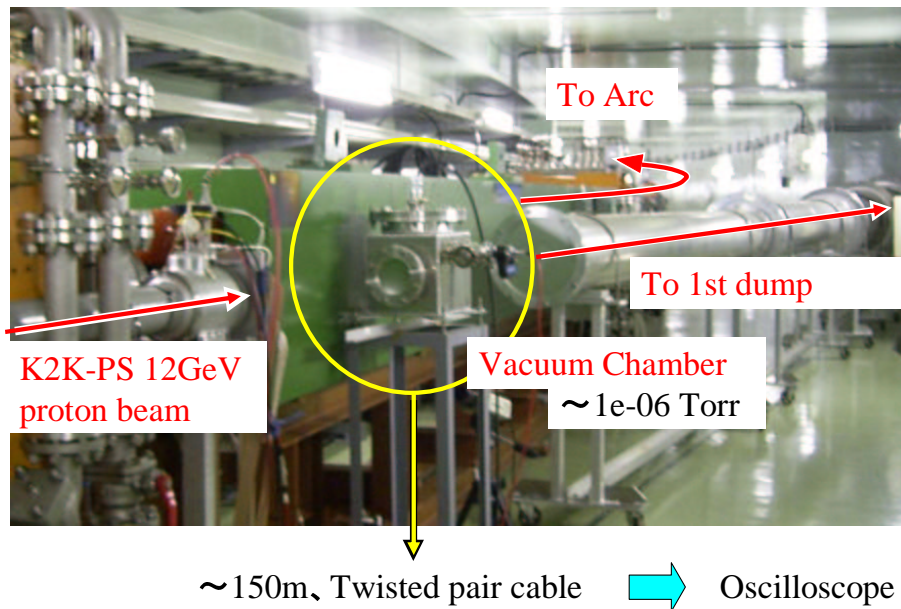


Figure 5.7: The setup of beam test. The SSEM is placed before the 1st dump in K2K neutrino beamline. The distance from read out system to this monitor is about 150m.

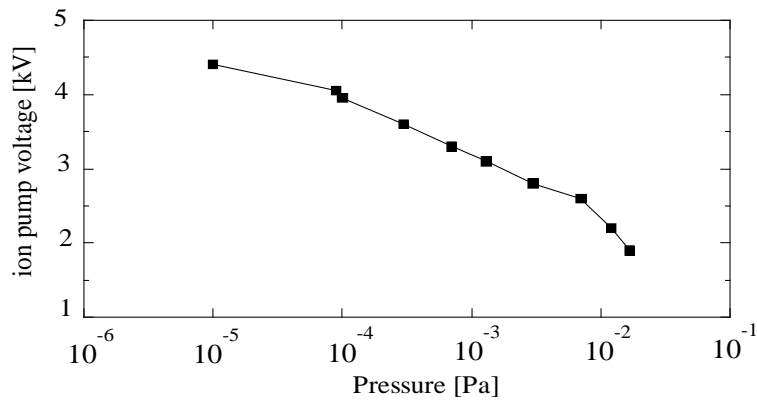


Figure 5.8: Vacuum dependence of ion pump voltage. Horizontal axis is the pressure measured by vacuum gauge, and vertical one is the voltage applied to the ion pump.

## The result of 1st beam test

- **Anode voltage dependence of signal height**

Figure 5.9 shows the anode voltage dependence of the signal height at the central channel of three copper cathodes. Signal height is saturated around 100V. In the following measurement, we set the anode voltage to 200V if it is not specified.

- **The measured wave forms with a oscilloscope**

Figure 5.10 shows the measured signal wave forms with oscilloscope. The top wave form is from SEM used in K2K as a beam intensity monitor. The lower 3 wave forms are signals from 3 aluminum channels in SSEM. 9 peak structure can be seen. This corresponds to the K2K beam structure. The peak piles up as it goes latter ones. The damping in cable is the cause of this pile up. There is a certain ingredient which comes before the signal from a beam. This ingredient synchronizes with the beam timing when the beam goes to Arc, i.e. when no beam pass through SSEM, and even when we disconnect the cables from monitor and just put them in the beamline. Therefore we think this is the noise, and is caused by the beam.

- **Difference between materials of cathode electrodes**

Figure 5.11 shows the measured beam profiles with three strips for each metal. The vertical axis of Fig.5.11 is the relative intensity of signals to the highest channel for each metal. We have set the beam shape to horizontally long and have changed the beam position from lower to upper. The measured profiles are responded to the beam positions, and do not depend on the cathode metals.

Figure 5.12 shows the measured secondary emission efficiencies for the 5 cathode materials. Black points are measured data, and blue squares are the result of the 70 MeV electron beam experiment performed at SLAC [14]. Error bars are the standard deviation of 9 measured values on each material. There exists some discrepancy between our results and the reference measurements at SLAC. Secondary emission efficiency depends on many factors as described above. Therefore further detailed studies are necessary to un-

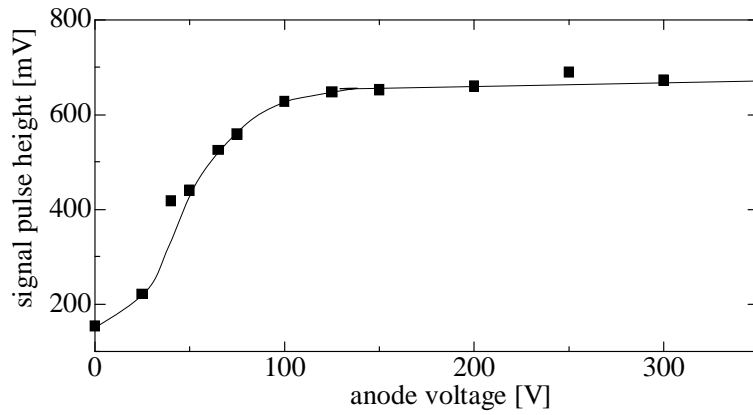


Figure 5.9: Anode voltage dependence of signal height. The signal is saturated around 100V.

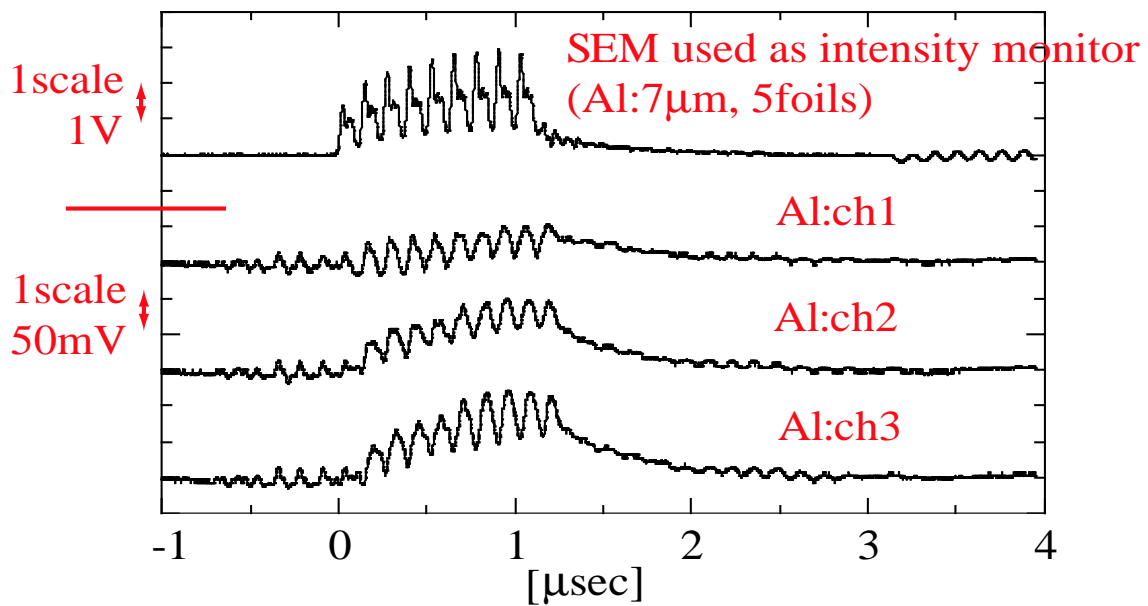


Figure 5.10: Waveform from aluminum three channels. The top wave form is signal from SEM used in K2K as a beam intensity monitor. The lower 3 wave forms are signals from three aluminum channels in SSEM.

derstand the discrepancy.

Anyway, all measured secondary emission efficiencies are in the same order. As for these 5 cathode materials, secondary emission efficiencies does not influence when we choose the material of cathodes.

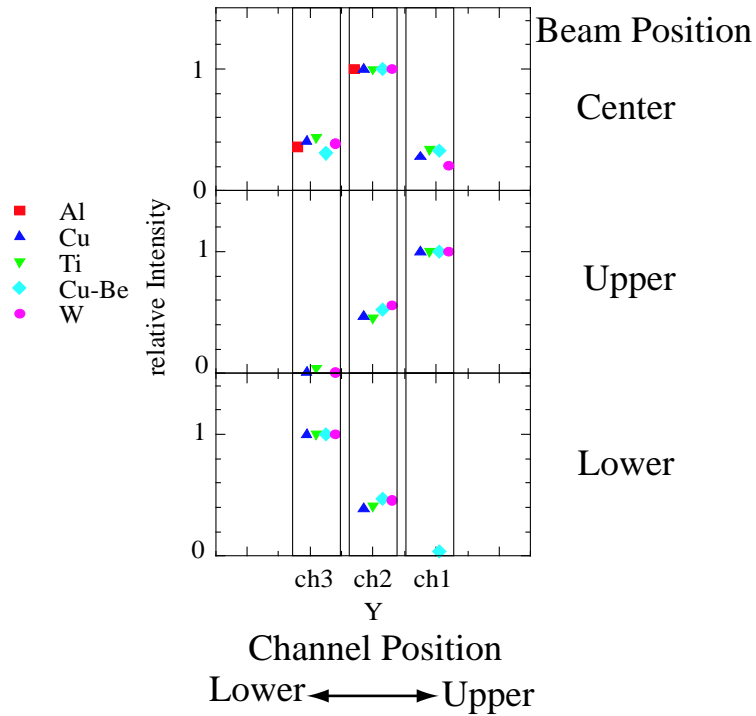


Figure 5.11: The measured beam profiles with three strips for each metal. Each metal is plotted with 5 different colors. The vertical axis is the relative intensity of signals to the highest channel for each metal, and in the horizontal, right side is the upper channel. From top figure, beam position is center, upper, then lower.

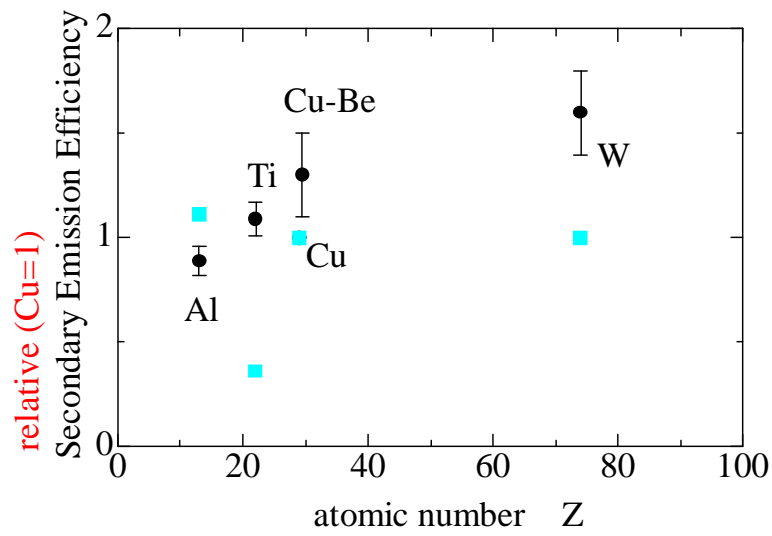


Figure 5.12: The measured secondary emission efficiencies for five cathode metals. Black points are measured data, and blue squares are the result from ref.[14].

### 5.3.2 The 2nd beam test

#### Design and setup

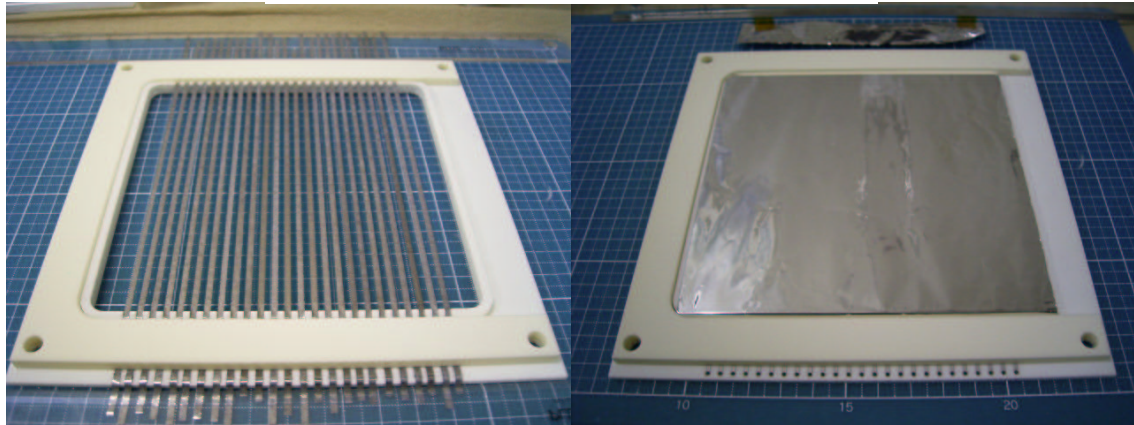
The purpose of this 2nd beam test is to test the fine segmented cathode electrodes. We have replaced electrodes in the vacuum chamber at the 1st beam test, with the titanium strips as shown in Fig.5.13. The width of strips is 2mm, thickness is  $5\mu\text{m}$ . The distance from the center of a cathode to the neighboring one is 4mm. In the current design, 25 titanium strips are placed on the ceramic board. For the convenience of readout connector and cables, we use 19 of the 25 strips. The 3 strips of the outside are used at the intervals of 8mm. The expected signal charge for the central strip is shown in Table 5.6. It is calculated with the same procedure as the equation 5.3 assuming that the beam shape is circle with the radius of 1cm. Anode electrodes are the aluminum foils also at this time. In this time, the distance between anode electrodes and a titanium strip cathode electrode is about 5mm.

Material	thickness [ $\mu\text{m}$ ]	material size interaction length [ $10^{-5}\lambda_{\text{int}}$ ]	signal charge [nC/pulse]
Ti (strip)	5	1.82	1.7 (center)

Table 5.6: Cathode materials for the 2nd beam test. The signal charge is estimated assuming that the beam shape is circle with the radius of 1cm.

For the multi-channel profile measurement, we have used the charge integration type ADC (LeCROY FASTBUS 1885n, 12bit), which is the part of K2K DAQ system. The gate width is about  $1.5\mu\text{m}$ . Timing of the gate is twice, one is synchronizing with the beam timing, and the other is about 1 second after the beam timing for the pedestal measurement. Full scale charge of this ADC is 1.6nC/channel, and the sensitivity is 400fC/count in high range mode. The input polarity of this ADC is negative, but SSEM signal polarity is positive. Therefore we have used the pulse transformer (EP101C-401, JPC) to invert the polarity of signals. In the K2K neutrino beamline, there is a SPIC, a beam profile monitor used in K2K, at one meter above the SSEM (Fig.5.7). We compare the beam profile measured by SSEM with ones by this SPIC.

Beam window : 12X12cm



Ti strip (2mm)

anode

Figure 5.13: Cathode and anode electrodes for the second beam test. Cathode electrode is made of the titanium strips with the width of 2mm. Titanium strips are placed with the gaps of 2mm on the ceramics base plate. Anode electrodes are made of aluminum foils again.

## The result of 2nd beam test

- Multi-channel profile measurement

Figure 5.14 shows the wave forms after the pulse transformer and 14dB attenuator. The lowest wave form is the gate for ADC. These inputs are integrated during the gating period.

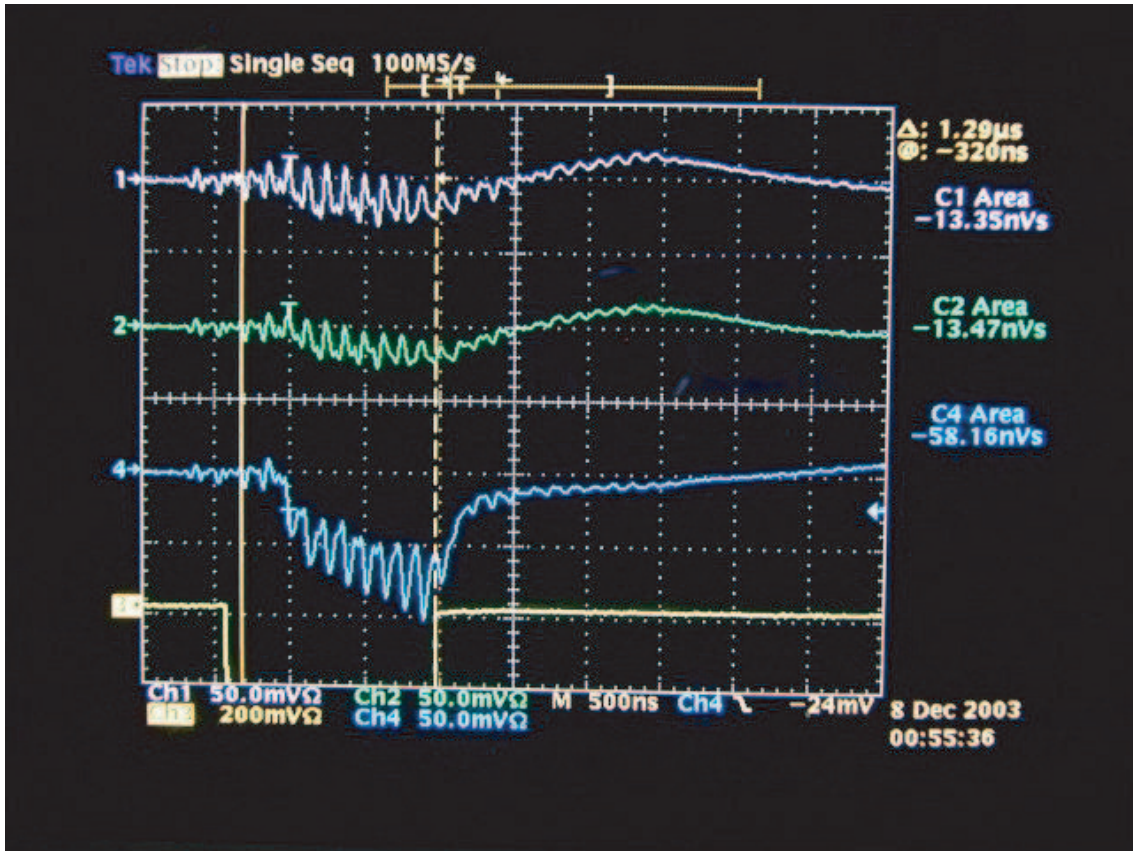


Figure 5.14: Signal wave form from titanium strips after the pulse transformer and 14dB attenuator. The position of these strips are 48mm, 16mm and 0mm left from the center of the base plate, respectively.

Note that during the measurement in the 1st beam test, vacuum was kept around the order of  $\sim 10^{-6}$  [Torr] (ion pump voltage is more than 4kV). However, the vacuum became worse to be around  $10^{-4}$ [Torr] (ion pump

voltage is 2.2kV), at the profile measurement with titanium strips. If the beam is in the Arc mode, i.e. no beam to this monitor, vacuum is kept in the order of  $10^{-6}$ [Torr]. We think that if beam passes through this monitor, gases are emitted from ceramic boards due to the radiation dose. Then vacuum become worse in tens of minutes. Even in this vacuum range, the behavior of SSEM looks unchanged and estimated charge of ionization is far less than that of secondary emission (Fig.5.2). We think it does not influence the behavior of SSEM so much in the current measurement.

Figure 5.15 shows the ADC data for 19 titanium strips. The pedestal data, which is taken every one second after the beam, is subtracted from data at the beam timing. Data of 9 channels out of 19, have not been taken properly. Some channels have disconnection of the ground line. Others are much noisy, although we do not understand the reason yet. We have taken away these data. With the remaining channels, we measure the beam profile and fit the profile with the Gaussian distribution. The result is shown in Fig.5.16. In order to see the response to the beam position changing, we measure the beam profiles for three beam positions. In this measurement, we use 20dB attenuator. In Fig.5.16, we show the measured profile with SSEM (upper figure) and that with SPIC measured at the same time as a reference (lower figure).

Table 5.7 is the relative center position of the beam, here the center position is obtained by the fitting to the profile with Gaussian. Table 5.8 is the value of one sigma of them. The result from SSEM and SPIC is different about 30%.

	left	center	right
SSEM	-16mm	0 (by definition)	+12mm
SPIC	-13mm	0 (by definition)	+14mm

Table 5.7: Change in the center position of measured beam profiles for three beam positions.

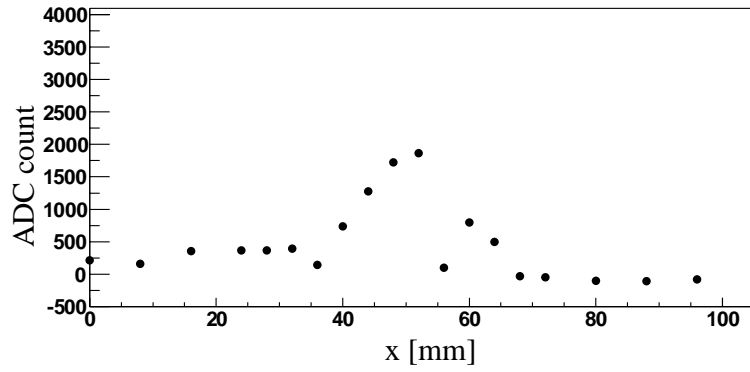


Figure 5.15: ADC count from 19 titanium strips.

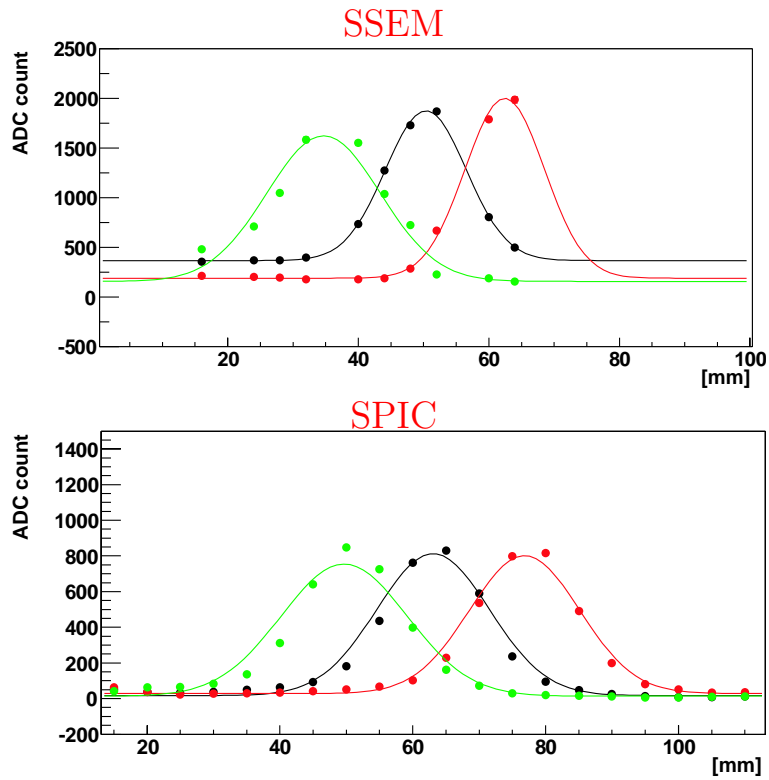


Figure 5.16: The measured beam profiles for three beam positions. We show the measured profile with SSEM (upper figure) and that with SPIC measured at the same time as a reference (lower figure).

	left	center	right
SSEM	8.7mm	6.2mm	6.1mm
SPIC	9.5mm	8.5mm	8.3mm

Table 5.8: The value of one sigma of each beam profile shown in Fig.5.16.

As for SSEM, some measured signal behaviors are not understood yet. The measured profile by SSEM has the offset of several hundreds in ADC count. This offset seems to depend on the beam induced signals, because this offset seems not to exist when no beam pass through this monitor. Figure 5.17 shows the anode voltage dependence of profiles. To check the stability of beam during the measurement, we also show the profile measured by SPIC at the corresponding time. According to the Fig.5.17, the offset depends on anode voltage. We do not understand this offset yet. To understand the detailed behaviors, for example this offset and the discrepancy of measured profile between SSEM and SPIC, we need further studies.

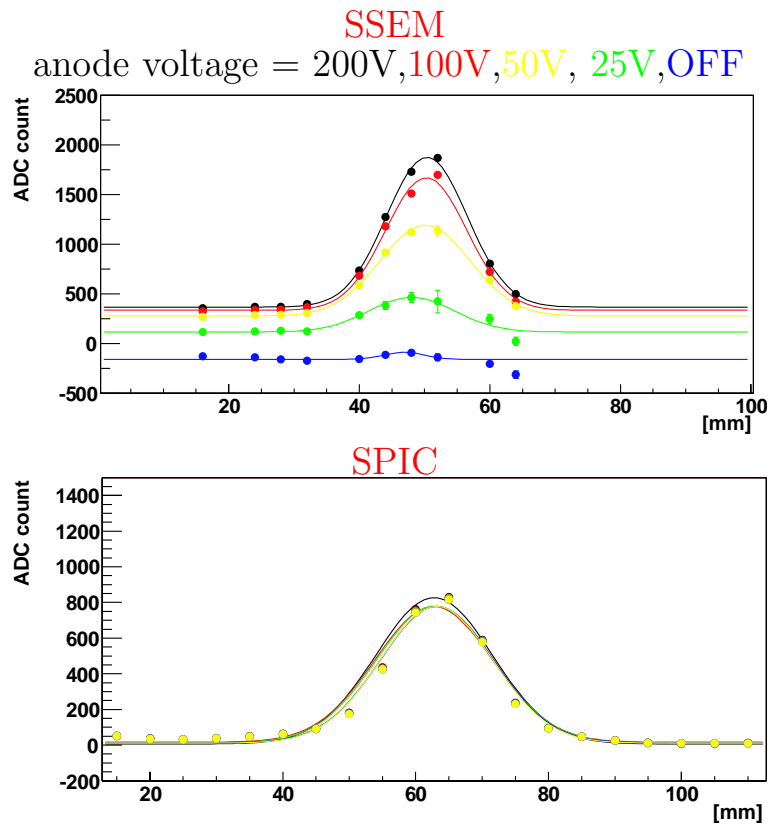


Figure 5.17: The anode voltage dependence of the measured profile.

## 5.4 Summary and Discussion

We have started the R&D of SSEM in the J-PARC neutrino beamline. The amount of material of SSEM is not so small to satisfy the beam loss limit in the arc section. We may need to reduce the area of electrodes interacting the proton beam. In terms of the amount of material, we prefer the smaller electrodes. However, the amount of signal charge depends on the size of electrodes. For the strip electrode, its width will be necessary at least 1mm for the beam intensity of  $10^{12}$  protons/pulse. For the wire electrode with the radius of  $\sim 50 \mu m$ , the amount of material will be in the same order as the 1mm wide strip, but the amount of signal charge seems to be smaller. We think the strips are preferable than wires.

We have carried out two beam tests of the SSEM at the K2K neutrino beamline. In the 1st beam test, we confirm the basic responses of the SSEM. We measure the secondary emission efficiencies in 5 cathode materials. The measured secondary emission efficiencies are in the same order in these 5 cathode materials. As for these 5 cathode materials, secondary emission efficiencies do not influence when we choose the material of cathodes. If we consider the amount of material, the mechanical strength and the high melting point, the titanium strip is the most preferable candidate.

In the 2nd beam test, we test the profile measurement using the fine segmented cathode electrodes made of titanium strips with the width of 2mm. The measured profile responses to the change of beam positions. We demonstrate the fundamental profile measurement performance with SSEM. However, the some signal behaviors remain not to be understood. We need further studies.

For the future SSEM R&D, the following issues should be studied:

- As for the lifetime of SSEM, we need to check the influence of the change of the secondary emission efficiency and to develop a calibration method.
- We should study whether a SSEM with holed anodes operate properly.
- We need to develop the movable structure to put the SSEM off from the beamline at usual operations.

- More detailed studies are necessary on the heating of electrodes.

After these basic tests, we will design SSEM for the J-PARC neutrino beamline.

# Chapter 6

## Conclusion

We have carried out the full beam line simulations for the J-PARC neutrino beamline designing. With the beamline simulations, we estimate the beam loss generated by the beam halo. In the current study, the total energy deposit in the arc section is as small as a few Watts, though this result may depend on the parameters of the incident beam halo, or the alignment errors of magnets and so on. We optimize the design parameters for some beamline components.

As for the collimator, our simulation result shows that the 5 cm thick iron gives nearly identical amount of radiation loss as the 50 cm thick iron. The radiation loss depends on the length of the collimators. It indicates the 5cm is thick enough, but length of the collimators must be maximized. The effect of the 5% smaller collimator gap size is small. Because in the preparation section, the major scraping of the beam halo takes place at the first four normal conducting magnets.

The simulation result also shows that in the preparation section, the radiation dose is large at these four upstream magnets and one steering magnet (named PV1). They may need to be built with the radiation resistant MIC magnets.

We also estimate the effect of the radiation shield at the exit of the preparation section. The result of current simulation does not favor the radiation shield at the exit of the preparation section, because the shield generates the secondary shower particles, which hit in particular the superconducting magnet immediately downstream the shield.

We have also carried out the R&D of the Segmented Secondary Emission

Monitor (SSEM) as a profile monitor for the J-PARC neutrino beamline. There are two beam tests of the SSEM at the K2K neutrino beamline. In the 1st beam test, we confirm the basic responses of the SSEM. As the material of cathode electrodes, we test the five metals. In these five cathode materials, the secondary emission efficiencies are in the same order. We think light material is preferable in terms of reducing the beam loss at the SSEM. At present, from the reasons of its mechanical strength and high melting point, we consider the titanium strip is the primary candidate for the cathode material. In the 2nd beam test, we use the titanium 2mm wide strips as the cathode electrodes, to test the beam profile measurement with fine segmented cathode electrodes. The measured profile has the response to the beam profiles. With this test, we demonstrate the fundamental profile measurement performance with SSEM. However, to decide the design of SSEM in the J-PARC neutrino beamline, we need more detailed studies. After these basic studies, we are going to decide the design of SSEM for the J-PARC neutrino beamline.

# Acknowledgement

I would like to express my heartfelt thanks to my supervisor H. Aihara. I am specially thankful to M. Iwasaki for her great advice.

I would like to express my appreciations to following people for their great help: H. Noumi, A. Ichikawa, Y. Yamanoi, Y. Hayato, T. Kobayashi, K. Agari, E. Hirose, Y. Sato, H. Takahashi, A. Toyoda, and all the other members of J-PARC Target Monitor Group. T. Ogitsu, Y. Iwamoto.

I am grateful to T. Higuchi, J. Tanaka, M. Yokoyama, T. Nakadaira, T. Tomura, N. Uozaki, and Y. Yamashita for their special support.

I also thank all the members in Aihara group, H. Kawai, A. Kusaka, R. Ishida, K. Itoh, Y. Nakahama, and H. Nakayama.

# Bibliography

- [1] Particle Data Group (2002).
- [2] M. Ishitsuka et al.(the Super-Kamiokande Collaboration) *Nuclear Physics A* **721** (2003), 509
- [3] M. H. Ahn et al.(The K2K Collaboration) *Phys. Rev. Lett.* **90** (2003), 041801.
- [4] Y. Itow et al. hepex/0106019 (2001)
- [5] "Letter Of Intent, Neutrino Oscillation Experiment at JHF", <http://neutrino.kek.jp/jhfnu/> (Jan,2003)
- [6] Y. Hayato et al. "J-PARC Neutrino Facility Technical Design & Development (Interim) Report"
- [7] S. Agostinelli et al. *Nuclear Instruments and Methods A* **506** (2003), 250
- [8] K. A. Brown et al. *Particle Accelerator Conferences Proceedigs '97* (1997), Session 8P 047
- [9] J. Camas et al. *CERN SL* 95-62 (1995)
- [10] V. Agoritsas. *CERN-MPS/Int.CO* 66-30 (1966)
- [11] A. R. BERDOZ, et al. *TRI-PP* 91-6 (1991); *Nuclear Instruments and Methods A* **307** (1991), 26
- [12] M. Ieiri, et al. "Response of KEK Secondary Emission Chamber to Several GeV Protons and Deuterons", The 9th Symp. on Acc. Sci. Tech., Tsukuba, Japan 1993.

- [13] Y. Yamanoi, private communication.
- [14] S.A.Blankenburger, et al. *Nuclear Instruments and Methods* **39** (1966), 303; *IEEE Transactions on Nuclear Science* **12** (1965), 935
- [15] B.Planskoy. *Nuclear Instruments and Methods* **24** (1963), 172
- [16] V. Agoritsas. *IEEE Transactions on Nuclear Science* Vol.NS-**26** (1979), 3355
- [17] G.Feroli. *CERN-SL* 97-71 (1997)
- [18] N.Hilleret et al. *CERN EST* 2002-003 (2002)